NAVAL POSTGRADUATE SCHOOL

MONTEREY, CALIFORNIA

THESIS

EXPLORING TURBULENT WAKES IN A NON-UNIFORMLY STRATIFIED ENVIRONMENT FOR SUBMARINE DETECTION

by

Elias D. Nadaf

June 2022

Thesis Advisor: Timour Radko
Co-Advisor: Justin M. Brown

Approved for public release. Distribution is unlimited.

THIS PAGE INTENTIONALLY LEFT BLANK

REPORT DOCUMENTATION PAGE			*Form Approved OMB No. 0704-0188*

1. AGENCY USE ONLY *(Leave blank)*	**2. REPORT DATE** June 2022	**3. REPORT TYPE AND DATES COVERED** Master's thesis

4. TITLE AND SUBTITLE
EXPLORING TURBULENT WAKES IN A NON-UNIFORMLY STRATIFIED ENVIRONMENT FOR SUBMARINE DETECTION

5. FUNDING NUMBERS

6. AUTHOR(S) Elias D. Nadaf

7. PERFORMING ORGANIZATION NAME(S) AND ADDRESS(ES)
Naval Postgraduate School
Monterey, CA 93943-5000

8. PERFORMING ORGANIZATION REPORT NUMBER

9. SPONSORING / MONITORING AGENCY NAME(S) AND ADDRESS(ES)
N/A

10. SPONSORING / MONITORING AGENCY REPORT NUMBER

11. SUPPLEMENTARY NOTES The views expressed in this thesis are those of the author and do not reflect the official policy or position of the Department of Defense or the U.S. Government.

12a. DISTRIBUTION / AVAILABILITY STATEMENT
Approved for public release. Distribution is unlimited.

12b. DISTRIBUTION CODE
A

13. ABSTRACT (maximum 200 words)

This study aims to explore the behavior of turbulent wakes generated by a spherical submerged body propagating with constant speed in a non-uniformly stratified fluid. The investigation is based on a series of high-resolution numerical simulations in which the background stratification is systematically varied. We consider one linear and five non-linear temperature profiles and two sets of Froude numbers (Fr), Fr = 1.0 and Fr = 3.2. The analysis of dissipation of thermal variance (χ) shows that the shape of the wake for non-uniform profiles is more horizontally spread, and internal waves are much stronger than in linear stratification. Experiments with Fr = 1.0 show a rather asymmetric energy distribution caused by internal wave reflections from low-gradient regions. An idealized model demonstrates that internal waves emitted at horizontal angles shallower than roughly 64 degrees are reflected. For Fr = 3.2, internal waves are radiated at steeper angles and transmitted more. Using decay rates of χ, the maximum detection time of the wake can be estimated, showing that for Fr = 3.2, the thermal signal lasts four to five times longer than for Fr = 1.0. Furthermore, concave profiles produce signals lasting approximately twice as long as those for linear profiles, whereas low-gradient types have half the duration. This research is expected to assist in the development of non-traditional detection algorithms for undersea warfare.

14. SUBJECT TERMS
wake dynamics, non-linear stratification, kinetic energy, thermal energy, dissipation rate of kinetic energy, dissipation rate of thermal variance, epsilon parameter, chi parameter, variations in temperature field, numerical modeling, openfoam, submarine detection, no acoustic means detection, internal waves reflection, Froude number, high-resolution numerical simulation, wake core position

15. NUMBER OF PAGES
67

16. PRICE CODE

17. SECURITY CLASSIFICATION OF REPORT	**18. SECURITY CLASSIFICATION OF THIS PAGE**	**19. SECURITY CLASSIFICATION OF ABSTRACT**	**20. LIMITATION OF ABSTRACT**
Unclassified	Unclassified	Unclassified	UU

NSN 7540-01-280-5500

Standard Form 298 (Rev. 2-89)
Prescribed by ANSI Std. 239-18

THIS PAGE INTENTIONALLY LEFT BLANK

Approved for public release. Distribution is unlimited.

EXPLORING TURBULENT WAKES IN A NON-UNIFORMLY STRATIFIED ENVIRONMENT FOR SUBMARINE DETECTION

Elias d. Nadaf
Capitão de Corveta, Brazilian Navy
BNS, Brazilian Naval Academy, 2009

Submitted in partial fulfillment of the
requirements for the degree of

MASTER OF SCIENCE IN METEOROLOGY AND PHYSICAL OCEANOGRAPHY

from the

NAVAL POSTGRADUATE SCHOOL
June 2022

Approved by: Timour Radko
Advisor

Justin M. Brown
Co-Advisor

Peter C. Chu
Chair, Department of Oceanography

THIS PAGE INTENTIONALLY LEFT BLANK

ABSTRACT

This study aims to explore the behavior of turbulent wakes generated by a spherical submerged body propagating with constant speed in a non-uniformly stratified fluid. The investigation is based on a series of high-resolution numerical simulations in which the background stratification is systematically varied. We consider one linear and five non-linear temperature profiles and two sets of Froude numbers (Fr), Fr = 1.0 and Fr = 3.2. The analysis of dissipation of thermal variance (χ) shows that the shape of the wake for non-uniform profiles is more horizontally spread, and internal waves are much stronger than in linear stratification. Experiments with Fr = 1.0 show a rather asymmetric energy distribution caused by internal wave reflections from low-gradient regions. An idealized model demonstrates that internal waves emitted at horizontal angles shallower than roughly 64 degrees are reflected. For Fr = 3.2, internal waves are radiated at steeper angles and transmitted more. Using decay rates of χ, the maximum detection time of the wake can be estimated, showing that for Fr = 3.2, the thermal signal lasts four to five times longer than for Fr = 1.0. Furthermore, concave profiles produce signals lasting approximately twice as long as those for linear profiles, whereas low-gradient types have half the duration. This research is expected to assist in the development of non-traditional detection algorithms for undersea warfare.

THIS PAGE INTENTIONALLY LEFT BLANK

TABLE OF CONTENTS

I. INTRODUCTION....1
A. MOTIVATION....1
B. BACKGROUND....1
C. SUMMARY OF WORK....5
D. ORGANIZATION....6

II. METHODS....7
A. NUMERICAL MODEL....7
B. EXPERIMENTAL SETUP....9

III. RESULTS....15
A. WAKE SIGNATURES....17
1. Wake Morphology....18
2. Wake Position....24
3. Wake Decay....26
B. INTERNAL WAVES....30

IV. DISCUSSION....41
A. CONCLUSIONS....41
B. OPERATIONAL RELEVANCE....41
C. FUTURE WORK....42

APPENDIX. TEMPERATURE PROFILES SYMMETRY....43

LIST OF REFERENCES....45

INITIAL DISTRIBUTION LIST....49

THIS PAGE INTENTIONALLY LEFT BLANK

LIST OF FIGURES

Figure 1. Wake of a near-surface submerged submarine. Source: Bureau of Naval Personnel (1953).....2

Figure 2. Stages of wake evolution. Source: De Stadler (2013). 4

Figure 3. Overview of the model configuration. This figure represents the initial state, so the body and inner box are centered at [0, 0, 0].....7

Figure 4. Outer mesh. 10

Figure 5. Inner mesh.....10

Figure 6. Linear Case and Cases 1–3 temperature profiles. 12

Figure 7. Case 4 and Case 5 temperature profiles. 13

Figure 8. Wake formation for Linear Case (Fr = 1.0). 15

Figure 9. Vertical and horizontal temperature perturbation fields for Linear Case and Case 1 (non-linear stratified case) in Fr =1.0 set.....16

Figure 10. Cross-sections of χ for Linear Case and Case 1 in Fr = 1.0 and Fr = 3.2 at Nt ~ 5. 19

Figure 11. Cross-sections of χ for Linear Case and Cases 1–3 in Fr = 1.0 at Nt = 25. 20

Figure 12. Cross-sections of χ for Linear Case and Cases 1–3 in Fr = 3.2 at Nt = 25. 21

Figure 13. Cross-sections of χ for Cases 4 and 5 in Fr = 3.2 at Nt = 25 and the respective Brunt-Väisäla frequency profile. 22

Figure 14. Cross-sections of ε for Linear Case, Case 1, and Case 5 for Fr = 1.0 and Fr = 3.2 at Nt = 25. 23

Figure 15. Vertical weighted mean position of the wake core as a function of time. 25

Figure 16. Quantitative analysis of wake decay for simulations with Fr = 1.0. 27

Figure 17. Quantitative analysis of wake decay for simulations with Fr = 3.2. 28

Figure 18. RKE.....32

Figure 19. Relationship between Brunt-Vaisala frequency profile and the presence of internal waves. 35

Figure 20. Reflection coefficient. 37

Figure 21. Distribution of specific kinetic energy emitted by IW as a function of the propagation angles. 40

LIST OF TABLES

Table 1. Summary of parameters defined for both sets. 13

Table 2. Parameters controlling the stratification pattern for each case. 14

Table 3. $\lambda\varepsilon$ and $\lambda\chi$ for all simulations. 30

Table 4. Maximum time for detecting turbulent and thermal signal. 30

Table 5. Estimated internal waves parameters. 39

THIS PAGE INTENTIONALLY LEFT BLANK

LIST OF ACRONYMS AND ABBREVIATIONS

3D	Near wake
CFD	Computational fluid dynamics
Fr	Froude number
IW	Internal waves
METOC	Meteorology and oceanography
NEQ	Non-equilibrium wake
OpenFOAM	Open-Source Field Operation and Manipulation
Q2D	Quasi-two-dimensional wake
Re	Reynolds number
RKE	Ratio of kinetic energy
SB	Submerged body

THIS PAGE INTENTIONALLY LEFT BLANK

ACKNOWLEDGMENTS

This challenging project is the result of the synergy of several efforts. First off, I would like to appreciate Dr. Timour Radko for his guidance and his kind and didactical manner. His unique experience, expertise and passion for fluid dynamics contributed greatly to my learning in the field. It has been an honor to collaborate with him for the last twenty months.

In the same manner, it has been a pleasure working with Dr. Justin Brown. He walked me through the CFD and greatly assisted in setting up the model correctly, making an unprecedented application for non-uniform stratification fields.

I am profoundly grateful to the Brazilian Navy for entrusting me with this expedition through knowledge. It was not only an opportunity to learn academic subjects, but also an unforgettable social and cultural experience.

My METOC colleagues—Alaina Ramsaur, Alexander Lehman, Emily Motz, Jason Dahl, Joel Harding—thank you for the camaraderie and respect that have always been given to me. Miguel Green, Monica Kiloran, and Shunika Johnson and their families, I am so grateful for making me feel at home and being a family to us. Our happy moments will always be in my best memories.

Lastly, I could not fail to express my deep gratitude to my family—my wife Christiane, and my daughters, Marina, and Giovana. They agreed to come with me in this endeavor and since then, they have supported me with love, care, and affection on this long two-and-a-half-year journey. I am deeply thankful for their understanding of my absences and for being patient throughout this time. I would not have made it to the end without you. You are the light and joy of my life. I love you.

THIS PAGE INTENTIONALLY LEFT BLANK

I. INTRODUCTION

A. MOTIVATION

The latest generations of quieter submarines have imposed new challenges for detection. Since acoustic and magnetic means may only find these objects in close proximity, recent research has aimed at the development of non-traditional algorithms for detection and tracking. One such avenue is the observation of the wakes generated by moving underwater vehicles. Therefore, several investigations based on laboratory, numerical, and observational experiments have been conducted to identify conspicuous features in the development and dynamics of wakes. However, the vast majority of numerical and theoretical wake models have assumed either homogeneous or linearly stratified density distribution, which do not represent the highly variable oceanic environment.

B. BACKGROUND

A moving submerged body traveling with high enough speed produces a turbulent wake in a fluid, and the characteristics of this disturbance depend on the properties of the body and the fluid. Figure 1 depicts a wake generated in the ocean by a submarine traveling at shallow depth and producing a noticeable perturbation at the sea surface. The characteristics of such wakes are often dependent on the Reynolds number (Re) of the flow, which measures the relative importance of viscosity and advection. In the context of wakes, the Reynolds number can be defined as

$$\mathrm{Re} = \frac{UD}{\nu}, \tag{1}$$

where U is the velocity of the body, D is the diameter of the body, and ν is the kinematic viscosity. At low Reynolds numbers ($\mathrm{Re} < \sim 2 \times 10^3$), the flow is laminar, and no turbulent mixing is present. A transitional regime from laminar flow to turbulent flow occurs when $2 \times 10^3 < \mathrm{Re} \leq 4 \times 10^3$, and the fully turbulent regime happens when

$\mathrm{Re} > 4 \times 10^3$. Typical Re values for surface vessels and submarines are approximately 10^8, so resolving turbulent scales at these high Re is nearly impossible for numerical simulations, at least with present computational capabilities (Zhou and Diamessis 2019). This is because the Kolmogorov length scale, η, which represents the scale in a turbulent flow at which turbulent eddies dissipate into heat, is controlled by Re ($\eta \sim \mathrm{Re}^{-3/4}$). Therefore, the higher the Reynolds number, the smaller the Kolmogorov scale will be, relative to the largest scales of the problem. This makes resolving both the large and small scales in numerical simulations difficult at high Reynolds number. In the more turbulent regime, the internal structure of the wake is characterized by many small-scale vortices; however, large-scale vortex streets are also created along the trajectory of the body and can be seen in both the laminar and turbulent regimes (Pao et al. 1982).

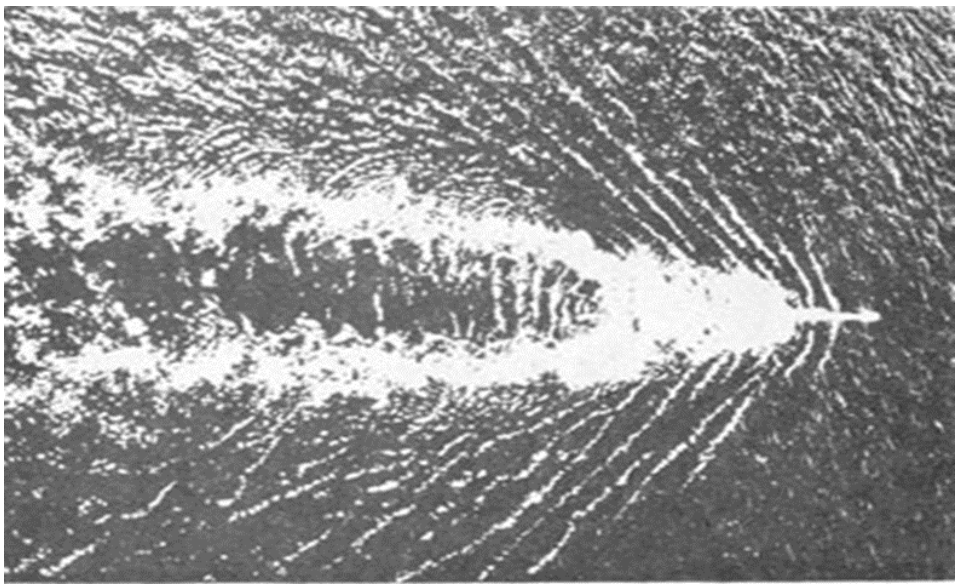

Figure 1. Wake of a near-surface submerged submarine. Source: Bureau of Naval Personnel (1953).

In a stratified fluid, the relationship between inertial forces and buoyancy can also be important to the development of the wake. This relationship can be described by the Froude number (Fr):

$$\mathrm{Fr} = \frac{U}{ND}, \tag{2}$$

where N is the Brunt-Väisäla frequency, the characteristic frequency for internal waves, which is defined as

$$N = \sqrt{\frac{-g}{\rho_0}\frac{\partial \rho}{\partial z}}, \tag{3}$$

where g, ρ_0, and ρ are the gravitational acceleration, reference density, and density, respectively. In the ocean, typical values for N are on the order of $3 \times 10^{-3} \mathrm{s}^{-1}$. The Froude number measures the ratio of the oscillation period of the internal waves to the wake decay time. When Fr is substantially larger than unity, the effects of stratification become less prominent, particularly at early times. The relevant timescale at which the stratification begins to impact the dynamics is the Brunt-Väisäla period (Lin and Pao 1979). After approximately one Brunt-Väisäla period after the start of the motion, internal waves emerge, emitted by both the body and turbulent motions in the wake. These internal waves serve to transfer energy from the wake to the surrounding medium, which promotes wake collapse (Spedding 2014). Stratification, therefore, plays an important role in wake dissipation, particularly at the late stages of wake development (Riley and Lelong 2000).

Spedding (1997) identified three distinct regimes of stratified wakes: namely, the turbulent 3D wake, the transitional non-equilibrium (NEQ) wake, and the quasi-two-dimensional (Q2D) wake. Figure 2 shows a schematic of those stages in the horizontal and vertical planes. The turbulent near-wake regime occurs when $Nt \leq 2$, where t represents the time after the passage of the object. Within that span of time, stratification effects are not yet significant, allowing the wake to expand vertically and laterally, as shown in laboratory experiments conducted by Hopfinger et al. (1991) and Xu et al. (1995). At $\mathrm{Nt} \sim 2$, buoyancy forces start to act significantly on the flow, and turbulent wakes stop growing vertically. At this point, wake collapse begins, and the wake decreases its vertical extent but continues to expand horizontally; this is the non-equilibrium stage and typically lasts from $2 < Nt < 50$ (Pao 1973). This motion converts potential energy into kinetic energy as the fluid approaches the level of neutral buoyancy.

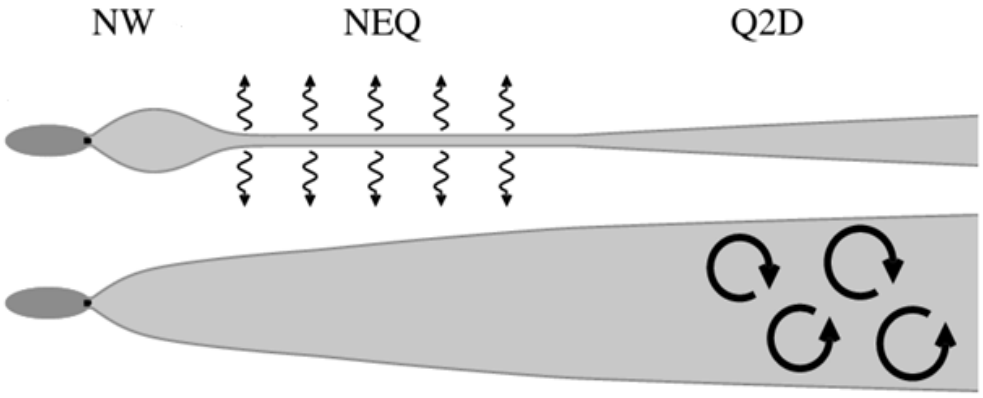

The vertical and horizontal directions, represented respectively by the top and bottom diagrams, show how the wake evolves over time. The moment when wake-generated internal gravity waves are prominent is shown by the winding arrows, and pancake eddies are seen in the late wake, which are represented by the circular arrows.

Figure 2. Stages of wake evolution. Source: De Stadler (2013).

During this process, internal waves transmit the energy away from the turbulent wake to promote wake collapse. As viscous dissipation destroys small-scale structures, the large and isolated coherent structures remain, which are known as pancake vortices (Radko and Lewis 2019). These pancake vortices are sustained much longer due to their coherent quasi-steady circulation patterns. This is the so-called Q2D regime, in which vertical motions are constrained and the wake flattens. This tendency is generally observed when $Nt > 50$ (Redford et al. 2015), although the actual transition is strongly dependent on Re. For example, Diamessis et al. (2011) and Zhou (2019) reported an extended NEQ regime for high Reynolds number ($\mathrm{Re} \geq 10^5$). At these late times, the Earth's rotation can become important (see the discussions from Spedding 2014; Sutyrin and Radko 2017; Radko and Lorfeld 2018).

Much of the energy dissipated from the wake during this process is due to the release of internal waves. In a homogeneous stratified environment, internal waves radiate in all directions and frequencies away from the path of a moving body (Keller and Munk 1970). They can be generated in two ways: fluid shifting away from the object as it passes through the medium (lee waves) or through random motions in the wake itself (random waves), as described by Rottman et al. (2004). Lee waves are the dominant form of internal waves for a spherical body moving through a stratified fluid when $\mathrm{Fr} < 4$, and random

waves are dominant at larger Fr (see discussions in Gilreath and Brandt 1985; Hopfinger et al. 1991). Abdilghanie and Diamessis (2013) examined near-field internal waves radiating from a towed sphere in a linearly stratified fluid at $\mathrm{Re} = [5 \times 10^3, 10^5]$ and $\mathrm{Fr} = [4, 16, \text{and } 64]$. They found that internal waves can persist until the extended NEQ regime (Nt ~ 100). Additionally, internal waves differ in their propagation angle depending on Re. At lower Re, waves radiate at a limited range of angles; however, at higher Re, wave propagation spreads over a larger range of angles, which results in a more efficient extraction of energy from the wake. Attempting to get a more realistic result in their numerical simulations, Brucker and Sarkar (2010) introduced a self-propelled object and compared its wake to that of a towed object in a stratified fluid. Their results supported that the energy transport provided by internal waves is of the same magnitude as the dissipation of turbulence, and the energy outflow carried by internal wave radiation dominates as a sink for kinetic energy. Zhou and Diamessis (2016) conducted numerical simulations to investigate how such far-field internal waves generated by a spherical submerged body in a linearly stratified fluid would affect the surface. They found that the most energetic waves, capable of reaching the surface are created in the early stages of the NEQ regime, when the wake is still being affected by stratification. However, as the system transitions to the Q2D regime, the internal wave intensity gradually reduces until viscosity serves as the major contributor to kinetic energy decay.

C. SUMMARY OF WORK

All the aforementioned work has been based on experiments with uniformly stratified or homogeneous fluid, which is not representative of typical ocean environments. Thus, this study focuses on a series of high-resolution numerical simulations in which the background stratification is systematically varied by locally perturbating the ambient density profiles to examine the impacts imposed by different stratification scenarios on turbulent wakes generated by a moving submerged body, including wake morphology, small-scale signature, internal waves distribution, and persistence. We find that the non-linear perturbations significantly affect the dynamics, persistence, and the detectability of wakes. It is observed that stratification anomalies can cause the wake to become vertically asymmetric. This asymmetry is attributed to the tendency of weak stratification to inhibit

the transmission of internal waves, which concentrates internal waves away from weakly stratified regions. Other wake characteristics that are strongly affected by the ambient stratification include the vertical position of the wake core and the persistence of the wake.

D. ORGANIZATION

The remainder of the thesis is organized as follows. In Chapter II, "Methods," the numerical model is introduced along with the governing equations and the model parameters. Chapter III, "Results," describes the diagnostics used for the model analysis and the achieved outcomes. Chapter IV, "Discussion," conveys the key conclusions and briefly summarizes our findings.

II. METHODS

This investigation is based on a series of numerical simulations in which a submerged body (SB), represented by a sphere, moves with constant speed inside a rectilinear domain. The domain has dimensions of 600m × 100m × 125m in the *x*, *y*, and *z* directions, respectively. The *x* (longitudinal), *y* (transverse), and *z* (vertical) directions represent, respectively, the orientations for length, width, and depth of both boxes. The *x*-axis extends through the range [-50m, 550m], the *y*-axis, [-50m, 50m], and the *z*-axis, [50m, -75m]. The body travels horizontally in the positive-*x* direction, starting its motion at [0m, 0m, 0m] with a speed of $u_b = 0.05\frac{m}{s}$ until x = 500m. The schematic of the simulated domain is shown in Figure 3.

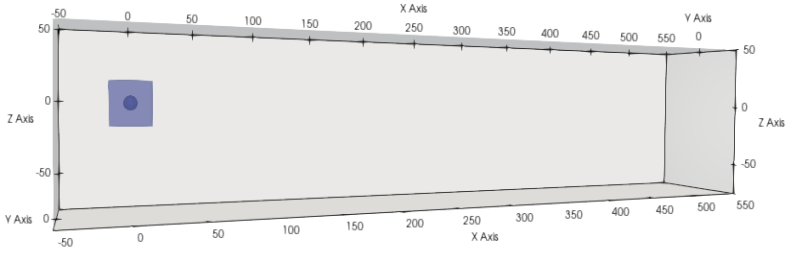

Figure 3. Overview of the model configuration. This figure represents the initial state, so the body and inner box are centered at [0, 0, 0].

A. NUMERICAL MODEL

We evolve the governing equations in the computational domain (Figure 4) to simulate the behavior of fluid around the body. Since the wake timescales are shorter than that of planetary rotation, the Coriolis effect is neglected. Furthermore, the simulations do not incorporate other external phenomena present in the ocean, such as waves, wind shear, and tides. Thus, the governing equations are as follows:

$$\frac{\partial \mathbf{u}}{\partial t} + \mathbf{u} \cdot \nabla \mathbf{u} = -\frac{1}{\rho_0}\nabla p + g\frac{\rho - \rho_0}{\rho_0}\hat{\mathbf{k}} + \nu_t \nabla^2 \mathbf{u}, \tag{4}$$

$$\frac{\partial T}{\partial t} + \mathbf{u} \cdot \nabla T = k_t \nabla^2 T, \tag{5}$$

$$\nabla \cdot \mathbf{u} = 0, \tag{6}$$

$$\frac{\rho - \rho_0}{\rho_0} = -\alpha_T (T - T_0), \tag{7}$$

where $\mathbf{u} = (u, v, w)$ is the total velocity vector, $\hat{\mathbf{k}}$ is the vertical unit vector, p is the pressure, T is the sea-water temperature, and T_0 is a reference temperature, which is set to be the surface temperature. Here, we use the Boussinesq approximation, for which the density perturbation to a constant reference density, ρ_0, is only retained in the buoyancy component of the vertical momentum equation. The thermal expansion coefficient, α_T, is set to $5 \times 10^{-5}\,^{\circ}\mathrm{C}^{-1}$, the gravitational acceleration, g, to 9.81m/s^2, the turbulent kinematic viscosity, ν_t, to 1×10^{-4}m^2/s, the turbulent diffusivity of heat, k_t, to 1×10^{-4}m^2/s, and the reference density, ρ_0, to 1024kg/m^3. The turbulent Prandtl number, P_{rt}, is defined as the ratio of the eddy viscosity to the turbulent thermal diffusivity, $P_{rt} = {\nu_t}/{k_t}$, which determines the relative efficiency of the vertical turbulent exchanges of momentum and heat. In this study, the turbulent Prandtl number is taken to be 1, which is consistent with the Reynolds analogy (i.e., in a turbulent flow, the turbulent eddies diffuse momentum and heat at equal rates).

The experiments are performed using OpenFOAM v2012, a free source software package (Weller et al. 1998). This model is chosen because it has a wide variety of wake modeling features, such as dynamic meshing and turbulence modeling capabilities. OpenFOAM is a finite-volume code, and for these simulations, an Euler scheme is used to evolve the equations forward in time using a PIMPLE algorithm (Holzmann 2019). Dynamic meshing and overset are enabled, which allows us to incorporate a moving mesh inside a stationary one and permits mesh movements and interactions without the drawbacks of deforming meshes (Tisovska 2019).

B. EXPERIMENTAL SETUP

The domain is discretized in terms of two independent meshes, one which simulates the bulk of the fluid and remains stationary (the outer box) and the other which simulates the fluid immediately around the body and which moves with it (the inner box). The inner box has dimensions of 30m × 30m × 30m and is centered on the body. The purpose of splitting the mesh into the outer and inner meshes is to create a composite domain that can resolve fine-scale structure near the submerged object while modeling the larger structures of the wake as they develop, allowing complex interactions between these structures. The inner mesh is overlaid on the outer mesh, and the external layer of cells in the inner mesh has values interpolated from the outer mesh as boundary conditions in order to solve the flow around the body with minimal communication between the two meshes. The fields from the closest cells to the body are then interpolated back to the outer mesh, which is then evolved independently.

The outer rectangular box is resolved by 1-m-grid spacing in the lateral directions but varying spacing in depth. In this perspective, the vertical domain is divided into three sections of different mesh resolution: I) The shallow section, extending from z = 50m to z = 25m, where the grid spacing contracts gradually from 3.5m at the surface to 0.42m at the bottom of the section; II) the intermediate section of constant resolution of 0.4m, which contains most of the wake and is restricted to the range z = [25m, -25m]; and III) the deep section, with z = [-25m, -75m], which also has non-uniform spacing from 0.4m on top to 3.46m on the bottom. The largest grid spacing of the inner box mesh is 0.5m in all three directions. However, within 2.5m of the submerged body, the grid spacing becomes more finely resolved by repeatedly dividing the grid cells into octants. As a result, each cell around the SB is 0.135m thick. The outer box has 10,560,000 (600 × 100 × 176) cells, and the inner box has 410,968 cells, including refinement levels. The outer and inner meshes are illustrated in Figures 4 and 5, respectively.

In the outer box, the top boundary is impermeable and stress-free, which adequately represents a wake of a body below the ocean surface in an open environment. The bottom boundary is open, while the temperature is prescribed, and the side boundaries are periodic.

The submerged body boundary is impermeable and non-slip, and the normal gradient of temperature is set to zero on all its surfaces.

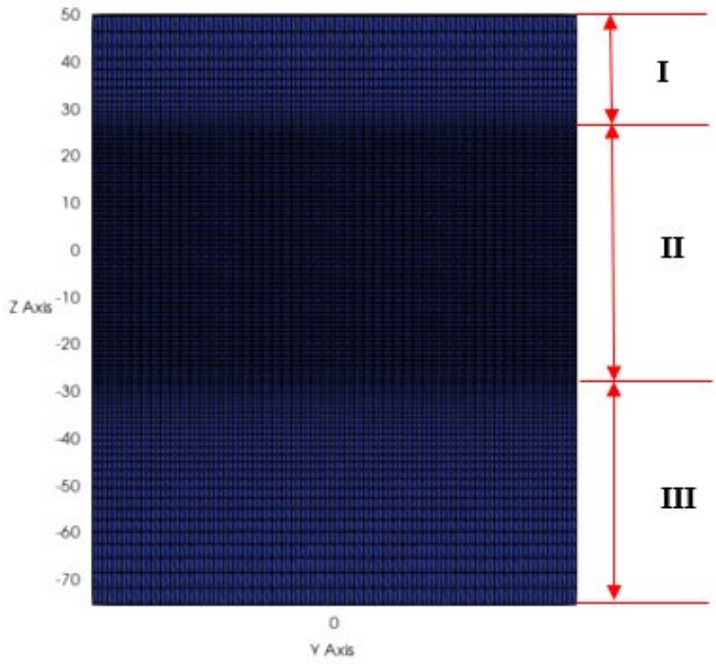

Vertical section (yz-plane) of the outer box mesh. From top to bottom: Shallow section (I), intermediate section (II), and deep section (III).

Figure 4. Outer mesh.

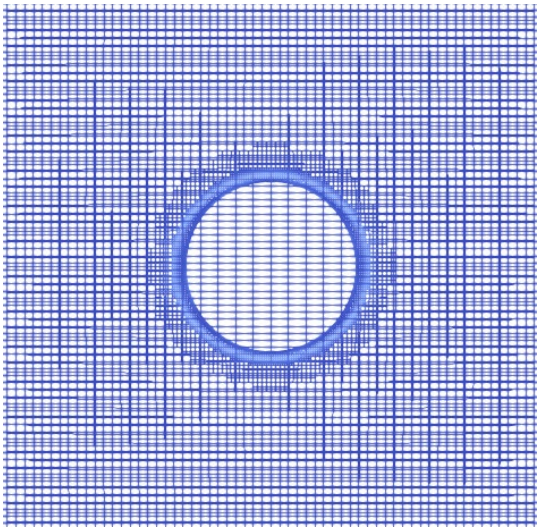

Vertical section (yz-plane) of the inner box mesh.

Figure 5. Inner mesh.

We perform two sets of simulations, characterized by $\mathrm{Fr} = 1.0$ and $\mathrm{Fr} = \sqrt{10}$ (~ 3.2), where the latter value of Fr was obtained by decreasing density gradient by a factor of 10. Each set contains six cases with different initial temperature profiles. For both values of Fr, the Reynolds number is Re = 5000. The six cases within each set comprise simulations with distinct temperature profiles, which we designate as the Linear Case (the case with constant stratification) and number the remaining cases as 1 through 5. For three of these—Case 1, Case 2, and Case 3—the temperature in the region is perturbed by a Gaussian as follows:

$$\bar{T}(z) = A_T z + \gamma \exp\left(\frac{-z^2}{\sigma^2}\right), \tag{8}$$

where $\bar{T}(z)$ is the vertical temperature profile, A_T is the unperturbed gradient of temperature, γ is the regulating parameter of the local temperature perturbation, and σ is the size scale of the perturbation. These profiles simulate the non-linear region as a density perturbation centered at the SB path. The stratification at the body depth is identical to that of the ambient fluid. Case 2 has the same internal curvature as Case 1 but with a stronger temperature perturbation, and Case 3 has the largest temperature perturbation and a stronger curvature, where curvature, *C*, is defined by

$$C = \frac{\partial^2 \bar{T}(z)}{\partial z^2}. \tag{9}$$

The purpose here is to quantify the role of curvature in wake development. Furthermore, all results obtained for Cases 1–3, for both values of Fr, are also valid for a vertically mirrored profile if the value of the parameter γ in Equation (8) takes the opposite sign and all other parameters remain the same. The isomorphism of the governing equation with respect to this transformation is demonstrated in the Appendix. The profiles for the Linear Case and Cases 1–3 are shown in Figure 6.

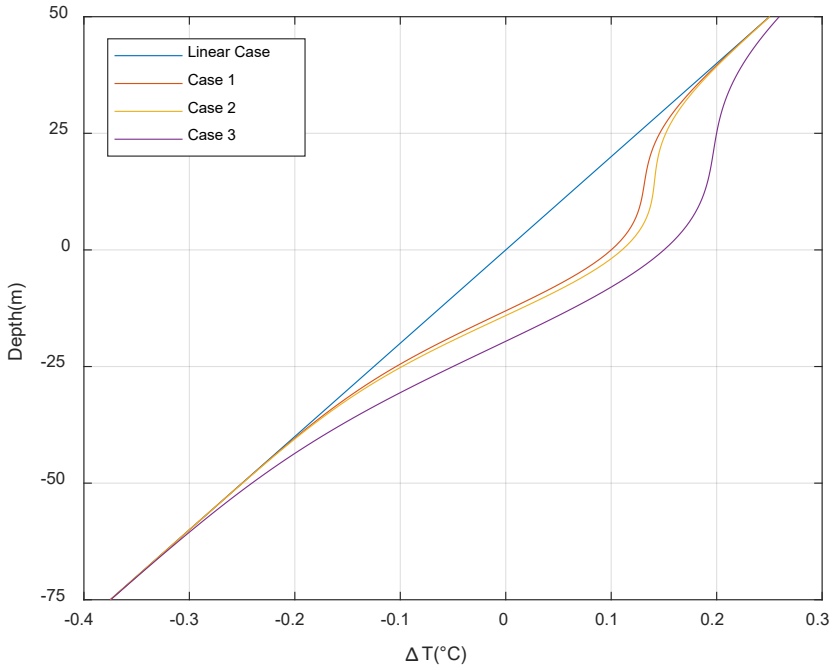

Figure 6. Linear Case and Cases 1–3 temperature profiles.

In Case 4, the non-linear region is represented by a high stratification along the SB trajectory, while Case 5 is characterized by a very low stratification in the same region. The profiles for Case 4 and Case 5 are depicted in Figure 7. These cases are described by

$$\bar{T}(z) = A_T z + \beta \tanh\left(\frac{z}{\delta}\right), \tag{10}$$

where β and δ control the inclination and size of the perturbed area. The parameters in common for both sets are summarized in Table 1, and the variables defined for each case are shown in Table 2.

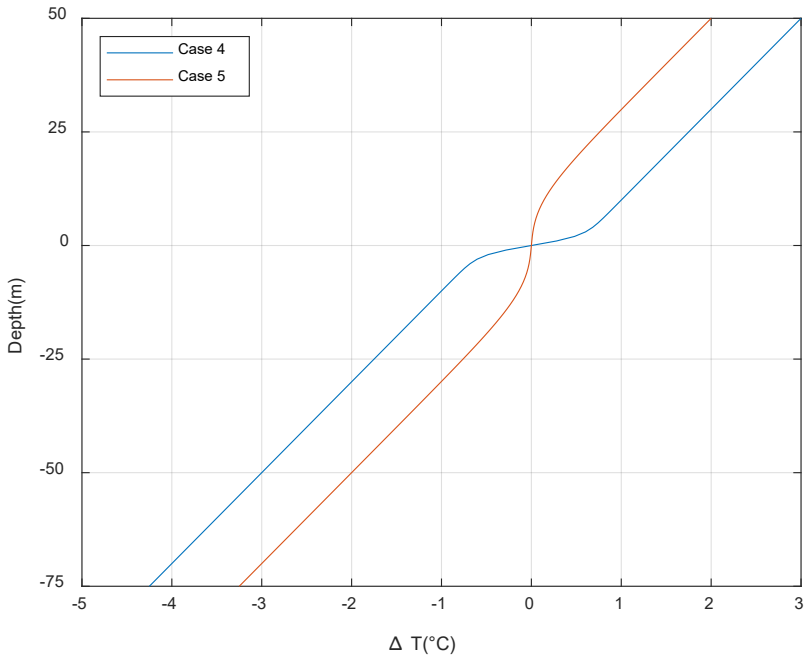

Figure 7. Case 4 and Case 5 temperature profiles.

Table 1. Summary of parameters defined for both sets.

Set	Re	$u_b\left(\frac{m}{s}\right)$	$\rho_0\left(\frac{kg}{m^3}\right)$	$\nu_T\left(\frac{m^2}{s}\right)$	$k_T\left(\frac{m^2}{s}\right)$	$\alpha_T\left(\frac{1}{°C}\right)$	$A_T\left(\frac{°C}{m}\right)$
Fr = 1.0	5×10^3	5×10^{-2}	1024	1×10^{-4}	1×10^{-4}	5×10^{-5}	1×10^{-2}
Fr = 3.2							1×10^{-3}

Table 2. Parameters controlling the stratification pattern for each case.

	Fr = 1.0				Fr = 3.2			
	$\gamma(°C)$	$\beta(°C)$	$\sigma(m)$	$\delta(m)$	$\gamma(°C)$	$\beta(°C)$	$\sigma(m)$	$\delta(m)$
Linear Case	0	-	1	-	0	-	1	-
Case 1	1	-	20	-	0.1	-	20	-
Case 2	1.103	-	21	-	0.1103	-	21	-
Case 3	1.5	-	30	-	0.15	-	30	-
Case 4	-	0.5	-	2	-	-0.5	-	2
Case 5	-	0.05	-	11	-	-0.05	-	11

III. RESULTS

Figure 8 depicts the formation of a wake along the SB's path in a linearly stratified environment. The turbulent wake begins to form immediately after the passage of the SB and thereafter spreads both vertically and horizontally. The wake is fully developed from approximately $x = 80$m up to the vicinity of the body, showing a turbulent core along its extent. The wake begins to flatten due to stratification, which can be seen for $x < 200$m, after expanding isotropically in the early stages. During the wake collapse, which usually occurs in the near-to-intermediate wake stage, the wake shrinks vertically and begins to expand horizontally. Additionally, internal waves can be seen past 200m, radiating out of the wake, and partially depleting its energy. In a uniformly stratified environment, the wake and internal wave propagation are vertically symmetric, but the introduction of perturbations could break the symmetry of the system.

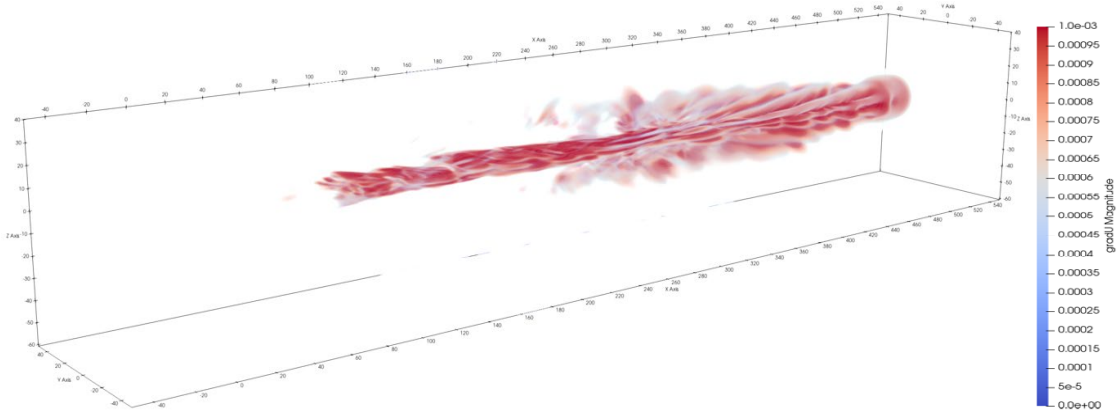

The wake core along the SB path and the internal waves radiating from the wake can be seen in the gradient of the velocity field. This figure shows the Linear Case, where the pattern of internal waves is symmetric.

Figure 8. Wake formation for Linear Case (Fr = 1.0).

Changes in the stratification affect the wake pattern, as well as the formation and propagation of internal waves. Figure 9 shows examples of the temperature perturbation field, $T' = T - \bar{T}$, in vertical and horizontal cross-sections. Here, we compare temperature signals from a linearly stratified (Linear Case) to a non-linear profile (Case 1) for Fr = 1.0.

For the case of the linear stratification, the wake signature is symmetrically distributed in z, whereas most of the signal is directed towards the bottom in the non-linear case. Conversely, the thermal signal spreads out more substantially in the horizontal direction for the perturbed case than for the case with linear stratification, which remains confined to the center. Therefore, preliminary evidence of changes in wake thermal signature from the introduction of nonlinearities in stratification led us to investigate more specific parameters that will be discussed below.

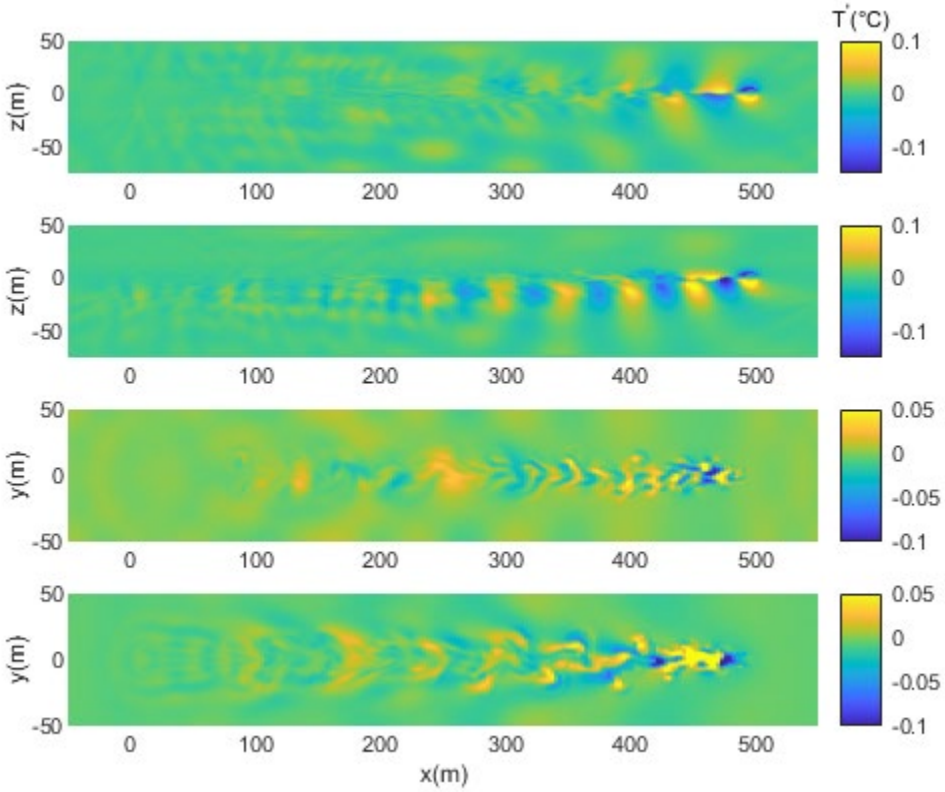

From top to bottom: Vertical cross-section of T' for the linearly stratified fluid; vertical cross-section of T' for Case 1; horizontal cross-section of T' for the linearly stratified fluid; and horizontal cross-section of T' for Case 1. All figures represent Nt = 25.

Figure 9. Vertical and horizontal temperature perturbation fields for Linear Case and Case 1 (non-linear stratified case) in Fr =1.0 set.

A. WAKE SIGNATURES

One of the measurable characteristics of a wake is the intensity of small-scale turbulence in its core, which is commonly quantified by turbulent and thermal dissipation rates. The dissipation rate of turbulent kinetic energy, ε, can be obtained from the turbulent kinetic energy equation and may be expressed as

$$\varepsilon = \nu_T \left[\left(\frac{\partial \mathbf{u}'}{\partial x} \right)^2 + \left(\frac{\partial \mathbf{u}'}{\partial y} \right)^2 + \left(\frac{\partial \mathbf{u}'}{\partial z} \right)^2 \right], \tag{11}$$

where $\mathbf{u}' = (u', v', w')$, and $\mathbf{u}' = \mathbf{u} - \bar{\mathbf{u}}$. Similarly, the dissipation rate of thermal variance due to diffusion of heat, χ, can be defined as

$$\chi = 2k_T \left[\left(\frac{\partial T'}{\partial x} \right)^2 + \left(\frac{\partial T'}{\partial y} \right)^2 + \left(\frac{\partial T'}{\partial z} \right)^2 \right]. \tag{12}$$

The thermal and turbulent dissipation rates offer independent and complementary descriptions of stratified turbulence. While they are frequently considered to be proportionate, this is not always the case (Gregg et al. 2018). Since the technology for measuring both quantities in field experiments is well-developed and widely used, a meaningful way to represent wake signals is to compute the dissipation rates of kinetic energy and thermal variance. These dissipation rates represent a potentially useful tool for detecting turbulent wakes (Radko and Lewis 2019). Because the small-scale signatures produced by the submerged body can be orders of magnitude greater than those produced by natural sources, it is much simpler to discriminate them from ambient processes than for large-scale wake signatures. The dissipation rates highlight small-scale features that are topologically connected to the wake-generating object. Thus, the dissipation rates of kinetic energy and thermal variance can be used for tracking of propagating submersibles.

1. Wake Morphology

Our analysis focuses on the behavior of the wake in the region from $x = 200\text{m}$ to $x = 300\text{m}$, far from the boundaries of the computational domain. This interval is the most representative region of the wake development in terms of wake size, evolution, and signal strength. The numerical simulations are extended for 10,000 seconds for the cases with Fr = 1.0, and 22,000 seconds for those with Fr = 3.2. In the following discussion, the wake evolution is described by referring to the non-dimensional time, *Nt*, which is a conventional approach in wake theory. Thus, the final values of *Nt* achieved in both Fr=1 and Fr=3.2 sets of simulations are identical.

We use dissipation rates to determine the wake structure and intensity and compare the morphology of various cases. We discover major dissimilarities in the wake evolution, its salient features, and propagation of internal waves between different cases. Figure 10 shows χ for the Linear Case and Case 1 with Fr = 1.0 and Fr = 3.2, when $Nt \sim 5$. Comparing the wakes for both Fr, we notice that the turbulent wake core is generally flattened by stratification over time. At higher Fr, the wake has had more time to expand due to turbulent dissipation prior to the onset stratification effects, and this can be observed at early stages. In addition, internal-wave (IW) radiation for the Fr = 1.0 cases is much more prominent than for the Fr = 3.2 cases. Besides, we start noticing from the early stages an asymmetric IW propagation for Case 1, which is mostly directed towards the bottom, in contrast to the more balanced IW propagation in the Linear Case.

In Figures 11 and 12, we plot χ in the *y*–*z* plane, averaged over the $200\text{m} \leq x \leq 300\text{m}$ range for the Linear Case and for Cases 1–3 with Fr = 1.0 and Fr = 3.2 at $Nt = 25$. In the Linear Case, we can clearly see the internal waves propagating symmetrically above and below the SB path. In Cases 1–3, the internal waves preferentially propagate downward, and few reach the surface. Particularly, Cases 1 and 2 are similar in terms of development, internal wave distribution, and strength. The evolution of Case 3 is distinct, and the differences become more prominent as Fr increases. In the simulations with Fr = 1.0, the wake core is more centralized, and its thermal signal does not fully extend to the surface. The signal strength in Case 3 is only slightly weaker than in Cases 1 and 2. In the simulations with Fr = 3.2, the wake in Case 3 is much stronger and spreads farther both

downward and horizontally in contrast to Cases 1 and 2. Note that the density profiles in Cases 1 and 2 have the same curvature and evolve in a similar manner. This suggests that the effect of the magnitude of the curvature, *C*, of the temperature perturbations plays an important role in the signal distribution, and those effects become more prominent as Fr increases.

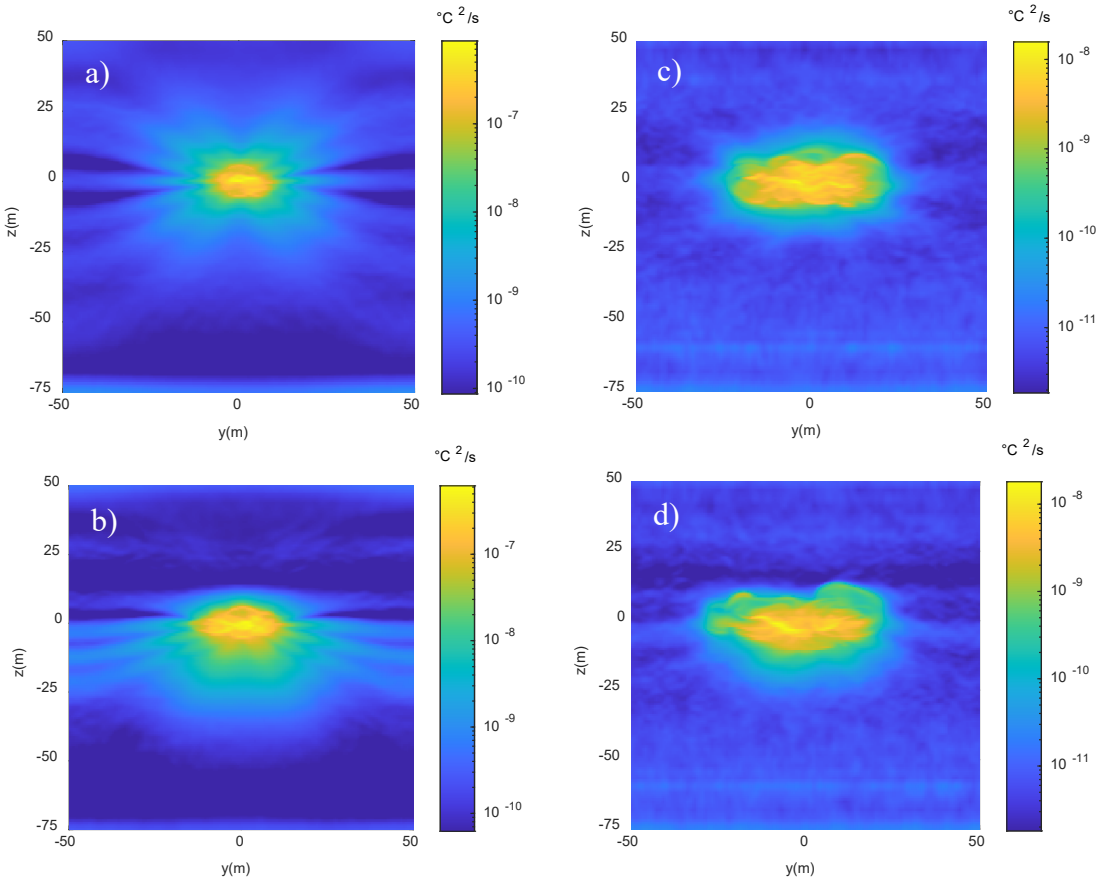

The *y*–*z* sections of the dissipation rate of thermal variance at Nt=5 for: a) Linear Case; b) Case 1 for Fr = 1.0, and c) Linear Case; d) Case 1 for Fr = 3.2.

Figure 10. Cross-sections of χ for Linear Case and Case 1 in Fr = 1.0 and Fr = 3.2 at Nt ~ 5.

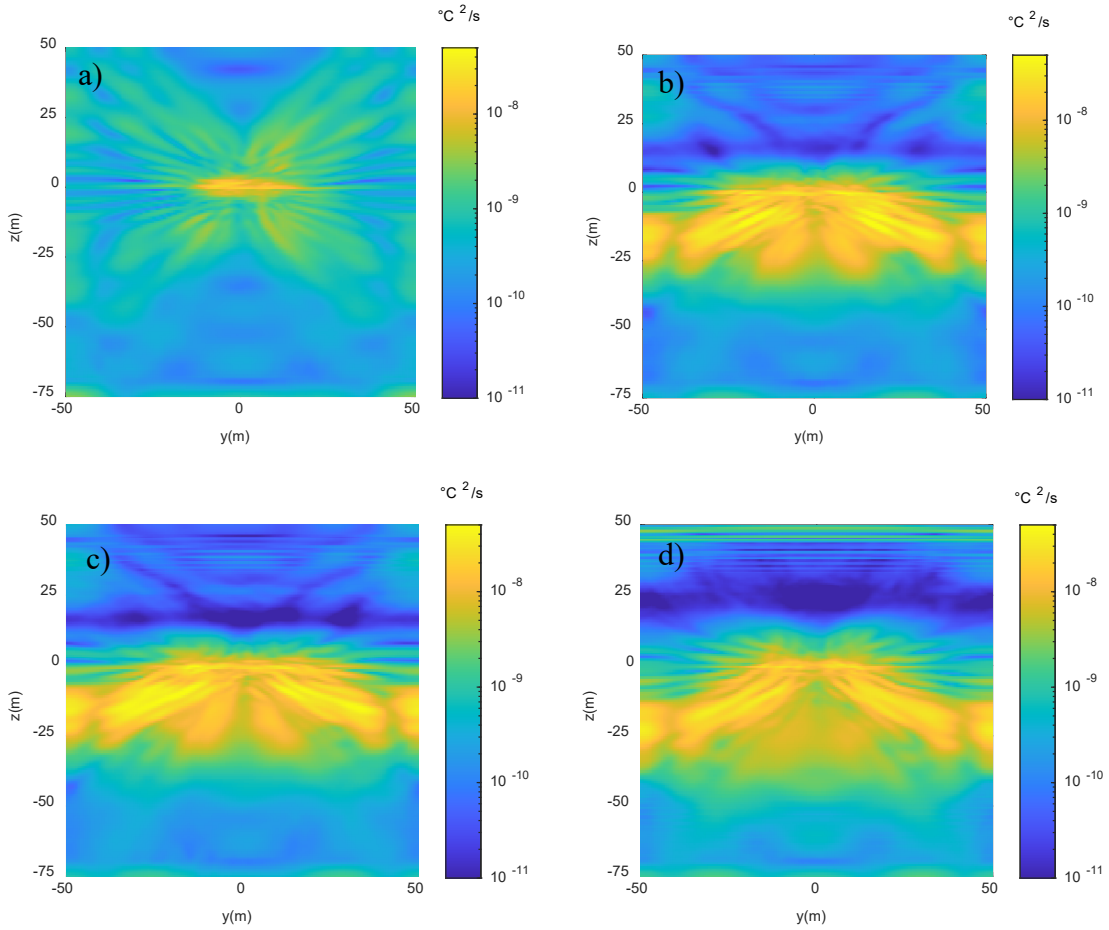

The *y*–*z* sections of the dissipation rate of thermal variance evaluated at Nt=25 for: a) Linear Case; b) Case 1; c) Case 2; and d) Case 3 for Fr = 1.0.

Figure 11. Cross-sections of χ for Linear Case and Cases 1–3 in Fr = 1.0 at Nt = 25.

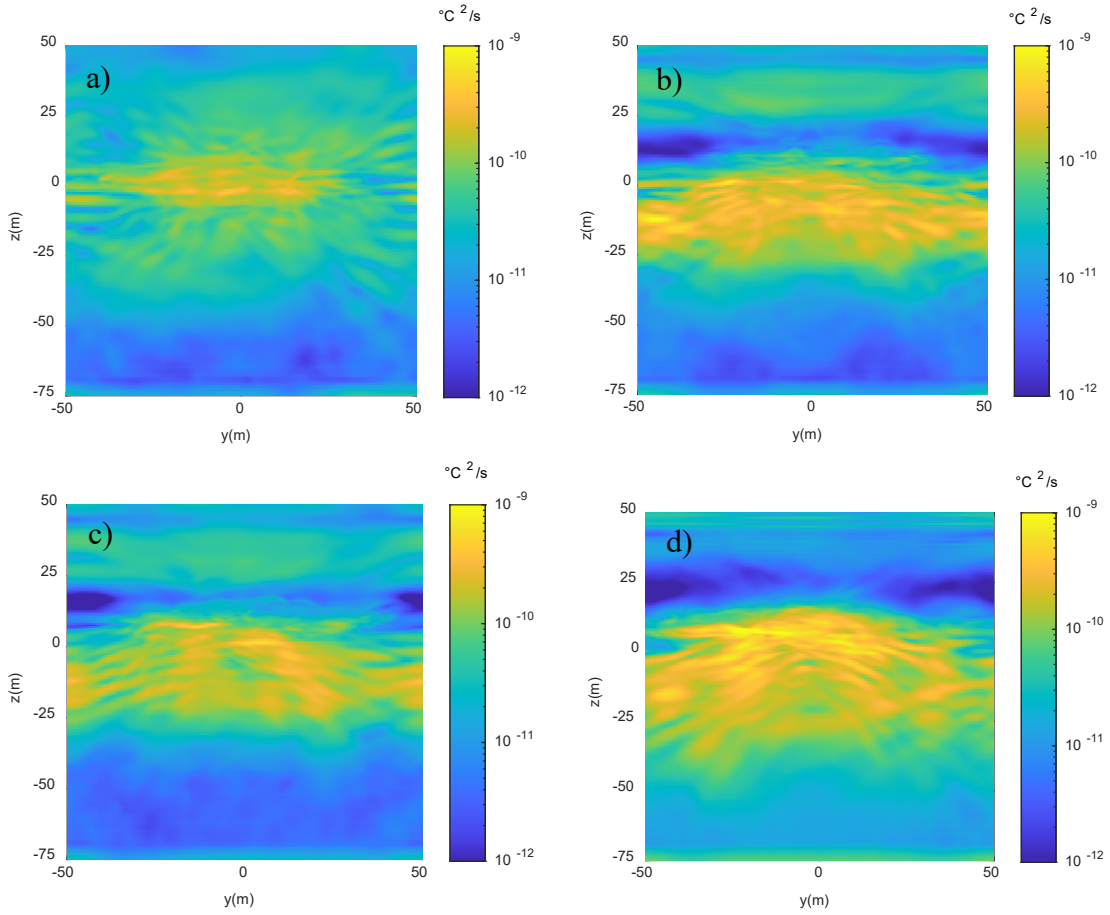

The *y*–*z* sections of dissipation rate of thermal variance evaluated at Nt=25 for: a) Linear Case; b) Case 1; c) Case 2; and d) Case 3 for Fr = 3.2.

Figure 12. Cross-sections of χ for Linear Case and Cases 1–3 in Fr = 3.2 at Nt = 25.

Figure 13 shows the same χ average for Cases 4 and 5 with Fr = 3.2 at $Nt = 25$. In these cases, the direction in which the thermal signal expands is closely related to the temperature gradient at the SB path. In Case 4, the local temperature gradient is large near the SB trajectory, and this increased stratification tends to suppress vertical motion, restricting the wake to the narrow region of z = [-5m, 5m]. This tendency promotes substantial lateral expansion during the wake collapse. Conversely, since Case 5 has the lowest gradient near the SB trajectory, the thermal signal can expand vertically and generates a more isotropic distribution in z = [-30 m, 30 m], as though the SB is moving through a homogeneous fluid. Nevertheless, the weak local gradient at the SB path causes

a very weak signal in the middle of the wake and precludes the wake from easily transmitting energy via internal waves. Cases 4 and 5 behave comparably at Fr = 3.2.

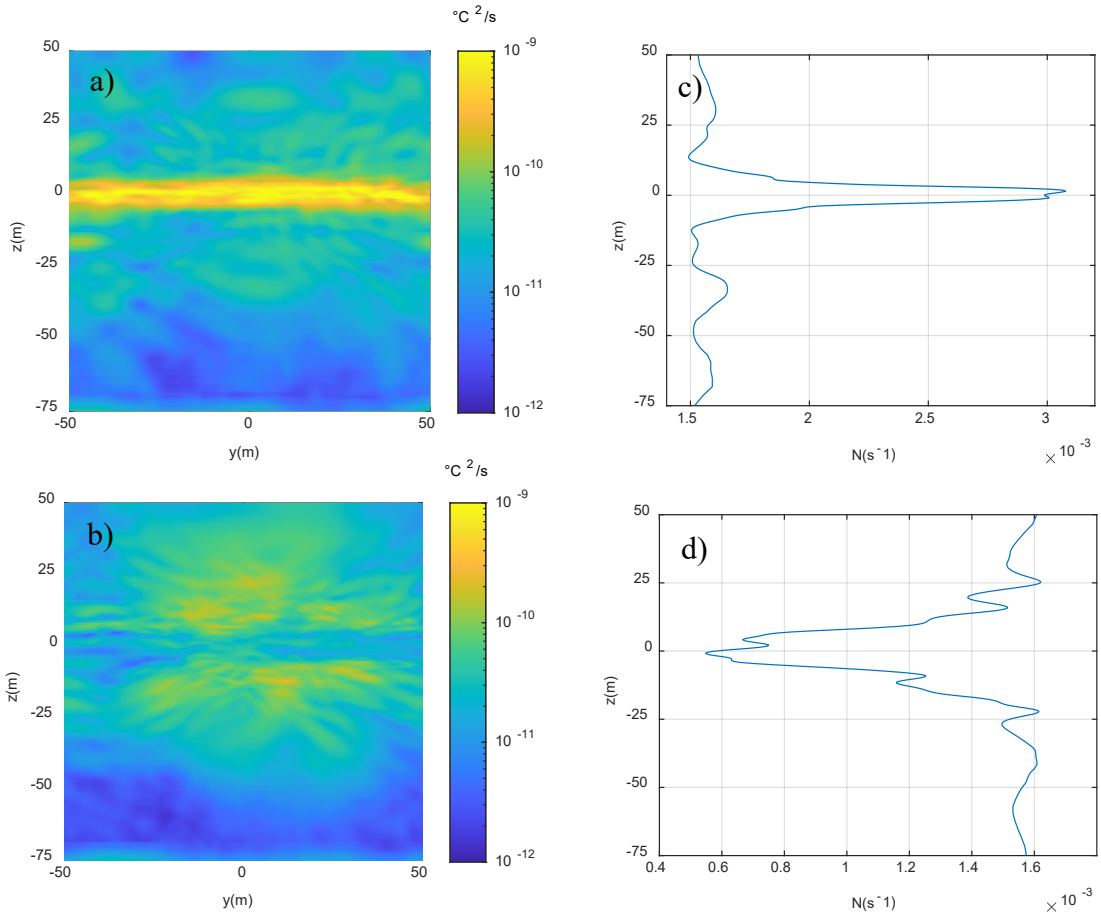

The *y*–*z* sections of the dissipation rates of thermal variance evaluate at Nt=25 for: a) Case 4; b) Case 5; c) *N* profile for Case 4; and d) *N* profile for Case 5 for Fr = 3.2.

Figure 13. Cross-sections of χ for Cases 4 and 5 in Fr = 3.2 at Nt = 25 and the respective Brunt-Väisäla frequency profile.

Figure 14 shows the turbulent dissipation rate for the Linear Case, Case 1, and Case 5 for both Fr = 1.0 and Fr = 3.2 at *Nt* = 25. Unlike the dissipation rate of thermal variance, the turbulent dissipation rate highlights the behavior of the turbulent wake rather than the internal waves. Thus, the kinetic signal is more coherent than the thermal signal and more concentrated around the SB trajectory. Likewise, the kinetic signal enhances the wake core, revealing the highly turbulent nature of wake cores in all cases. Although the kinetic signal is more spatially

distributed, the ε signal shows that the wake core is generally located near the axis of the SB path. Nevertheless, upward displacements are evident for cases with higher Froude numbers.

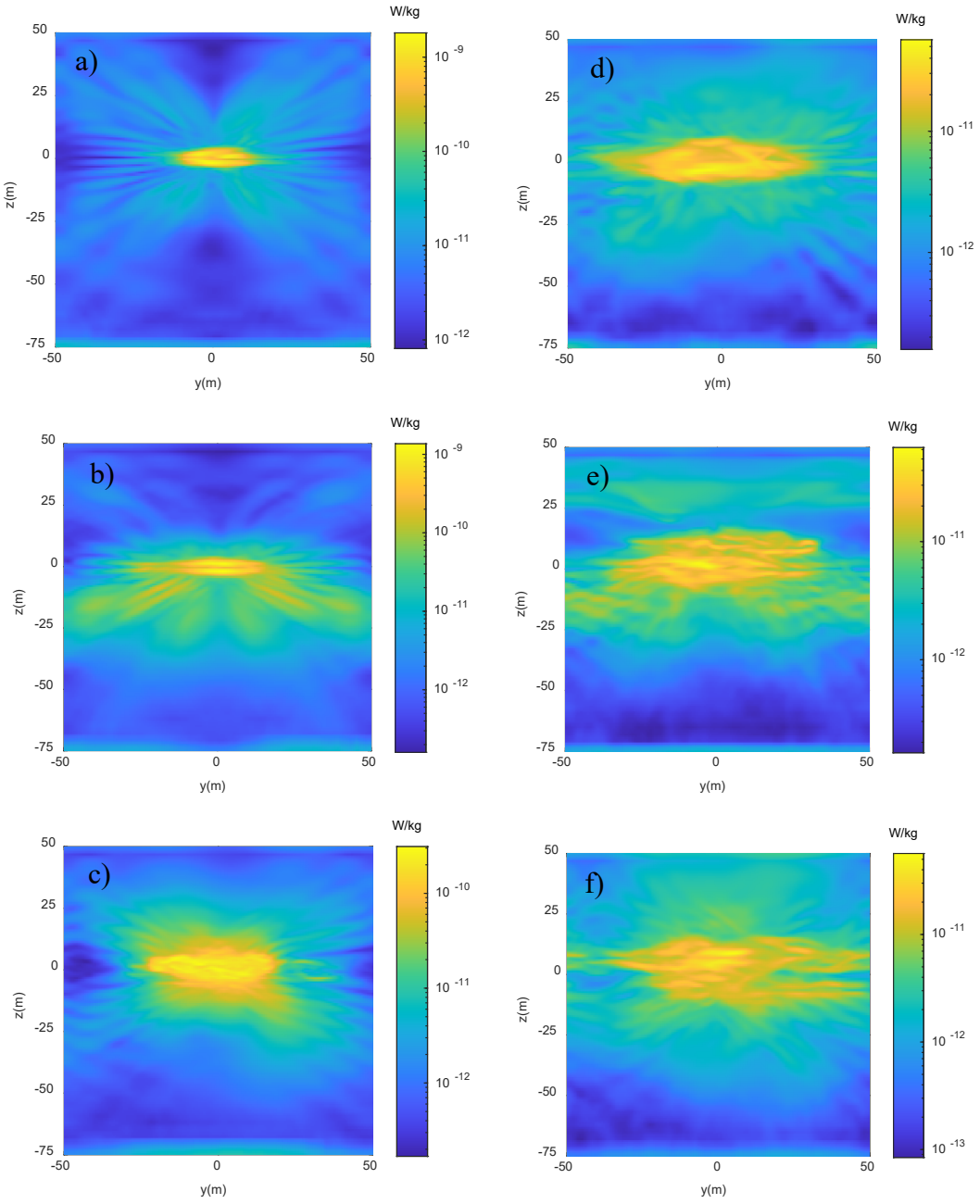

The *y*–*z* sections of turbulent dissipation rates evaluated at Nt=25 for: a) Linear Case for Fr = 1.0; b) Case 1 for Fr = 1.0; c) Case 5 for Fr = 1.0; d) Linear Case for Fr = 3.2; e) Case 1 for Fr = 3.2; and f) Case 5 for Fr = 3.2.

Figure 14. Cross-sections of ε for Linear Case, Case 1, and Case 5 for Fr = 1.0 and Fr = 3.2 at Nt = 25.

2. Wake Position

Though in a uniform stratification, the wake typically remains near the trajectory of the object due to the symmetry of the problem, this is not guaranteed for varying stratification. We use the specific kinetic energy to identify the turbulent regions of the wake to measure this vertical drift. Therefore, the center of the wake, $Zc(t)$, evaluated over the interval $200\text{m} \leq x \leq 300\text{m}$, is defined by the weighted mean expression

$$Zc(t) = \frac{\iiint_{x=200}^{x=300} \mathbf{u^2} z dV}{\iiint_{x=200}^{x=300} \mathbf{u^2} dV}, \tag{13}$$

where dV is the volume differential. For these calculations, only the most turbulent area around the wake core, which contains most of the signal and fits the actual core, has been selected. Those areas consist of rectangular regions between $-7\text{m} \leq \text{z} \leq 7\text{m}$ and $-15\text{m} \leq \text{y} \leq 15\text{m}$ for cases with Fr = 1.0, and $-12\text{m} \leq \text{z} \leq 20\text{m}$ and $-20\text{m} \leq \text{y} \leq 20\text{m}$ for Fr = 3.2.

Figure 15 shows the evolution of Zc in both sets of simulations. In early stages of the simulations with Fr = 1.0, the vertical position of the center is essentially identical for all cases. After that, Zc does not change appreciably in time and is generally located on the SB motion axis. In this case, the stable position of the wake indicates that the temperature anomalies have a small effect on the wake location, and the strong stratification keeps the wake tightly around the center for low Fr. For the simulations with Fr = 3.2, the wake drifts upward over time, stabilizing by *Nt* ~ 15 at a few meters higher than its original position; however, the various cases show a wider breadth of final values than those with Fr = 1.0. This suggests that as the stratification decreases, the nonlinear perturbations can increasingly affect the wake drift.

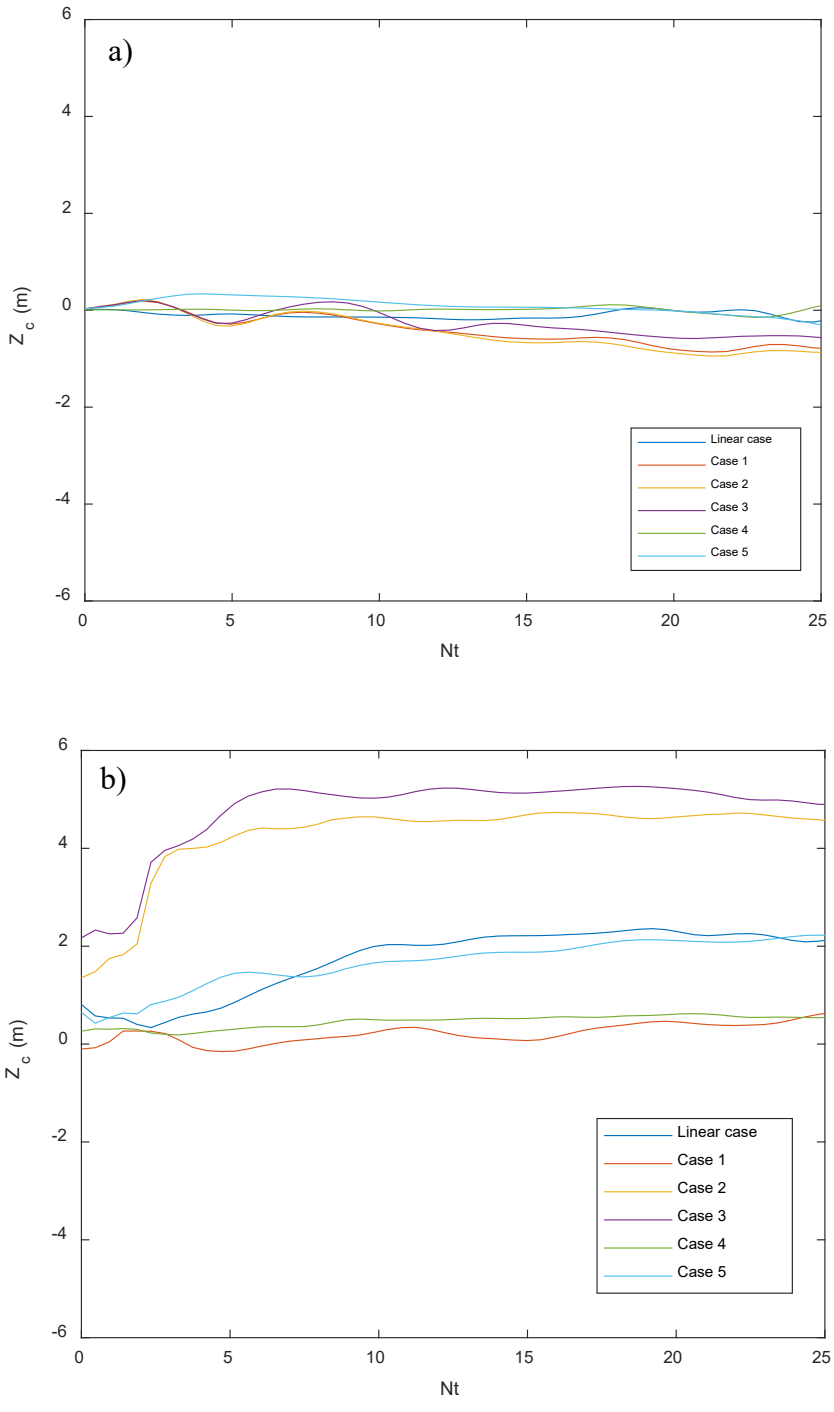

Vertical drift of the center of the wake. Figure a) represents cases with Fr = 1.0, and Figure b) Fr = 3.2.

Figure 15. Vertical weighted mean position of the wake core as a function of time.

3. Wake Decay

Figure 16 shows how the typical values of the maxima of χ and ε vary in time for the simulations with Fr = 1.0, and Figure 17 shows the same parameters for Fr = 3.2. These quantities are determined by averaging the local maxima in the wake in the *x*-direction for $200\text{m} \leq x \leq 300\text{m}$, as $\frac{1}{b-a}\int_{x=a}^{x=b} \max\left[f(x,y,z,t)dx\right]$, where $f(x,y,z,t)$ is the parameter of interest, and the max function is applied in *y* and *z* only. The minimum detection threshold is also shown, as established by Peterson and Fer (2014).

For the simulations with Fr = 1.0, the turbulent dissipation rate begins on the order of 10^{-6} W/kg for all cases and shows a monotonic decay after $Nt \sim 2$, having a smaller temporal variability for all cases after $Nt \sim 8$. In Case 4, the turbulence is constrained to the high-gradient region, and in Case 5, the turbulence spreads throughout the entire mixed-layer region. These simulations thus become the most and least turbulent cases, respectively, and have the highest and the lowest turbulent dissipation rates by the end of simulation. The kinetic dissipation rate for the simulations with Fr = 3.2 starts near 10^{-6} W/Kg for all cases, but for these, the power-law decay begins earlier, after Nt ~ 0.8. The general trends of all simulations are consistent with some stochastic variability. These evolutionary patterns are typical of previously reported wake experiments, with the turbulent dissipation rate being greatest right after the object's passage, when the wake turbulence is most intense (see, e.g., Radko and Lewis 2019).

The thermal variance dissipation rate shows a substantial dependence on the initial temperature profile. The simulations with Fr = 1.0 start from a range of approximately 10^{-8} °C^2/s (Case 5) to 10^{-5} °C^2/s (Case 4) and χ increases slightly until approximately $Nt \sim 3$ for all cases except for Case 5, in which the growth continues until $Nt \sim 8$. The remaining cases, the Linear Case and Cases 1–3, have comparable dissipation rates. For Fr = 3.2, the thermal signal has the same variation in magnitude between the individual cases as those shown for the simulations with Fr = 1.0, but for these, the highest and lowest thermal signal are two orders of magnitude smaller, ranging from 10^{-7} °C^2/s to 10^{-10} °C^2/s. The thermal signal peaks are approximately at $Nt \sim 2.5$ for all cases except for Case 5, which has the largest increase in amplitude and takes longer for it to peak, roughly at $Nt \sim 4$. The Linear

Case and Cases 1–3 have similar thermal signals until $Nt \sim 8$, where Case 3 deviates from the rest, decaying more slowly.

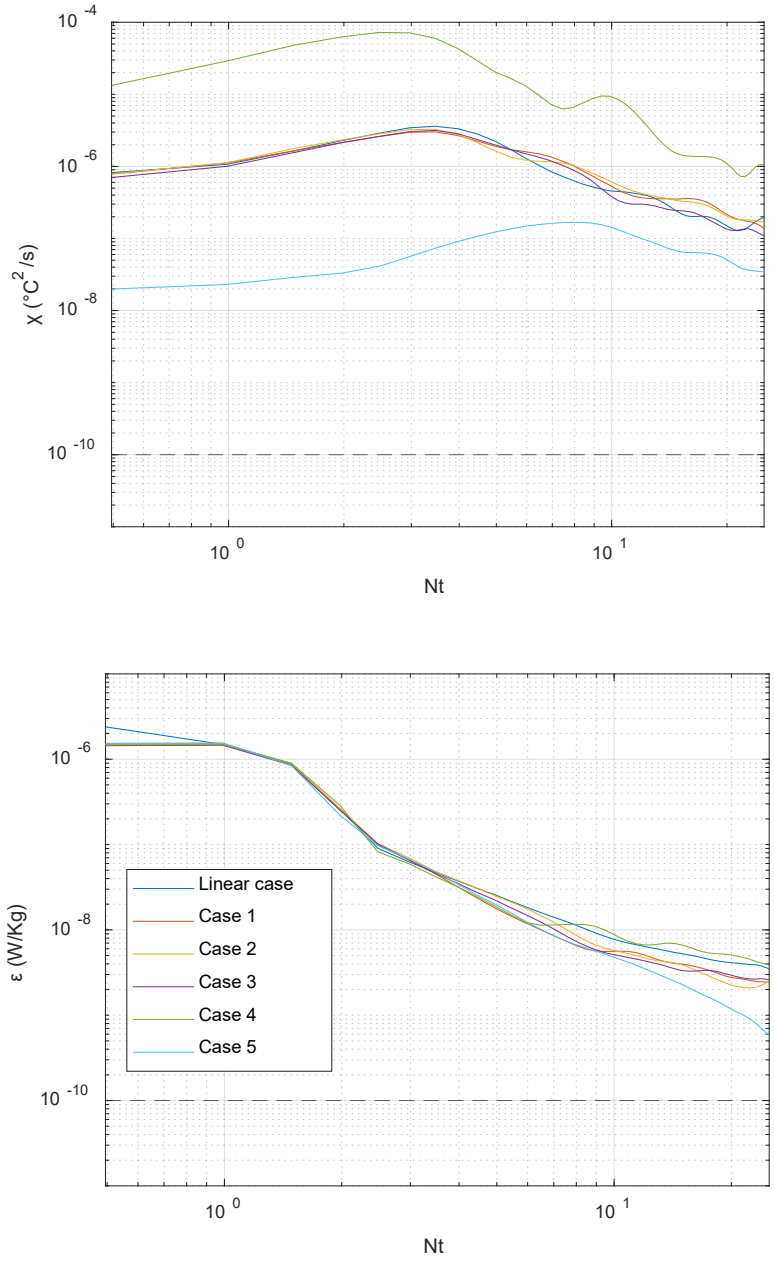

The upper panel shows the dissipation rate of thermal variance, χ, and the lower panel shows the dissipation rate of kinetic energy, ε, over time. The horizontal dashed line is the minimum threshold for signal detection.

Figure 16. Quantitative analysis of wake decay for simulations with Fr = 1.0.

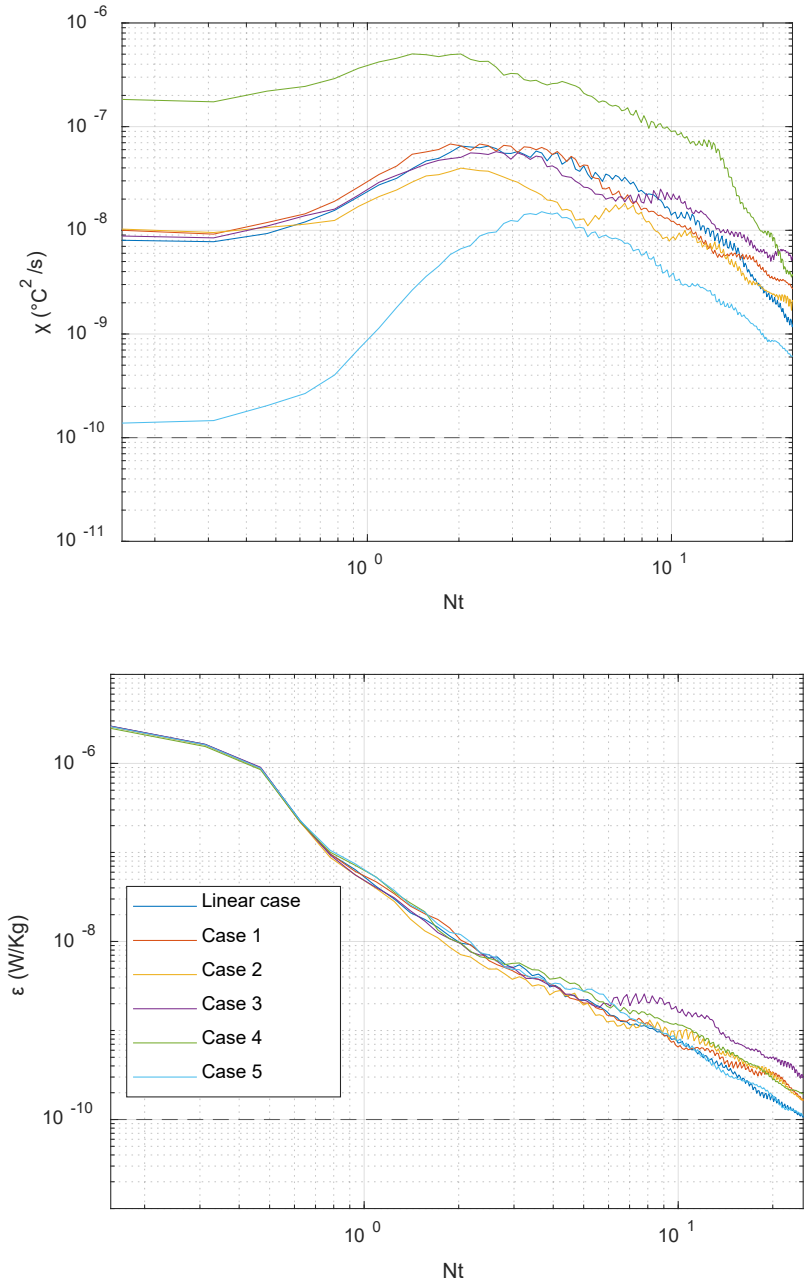

The upper panel shows the dissipation rate of thermal variance, χ, and the lower panel shows the dissipation rate of kinetic energy, ε, as functions of time.

Figure 17. Quantitative analysis of wake decay for simulations with Fr = 3.2.

The decay rates of turbulent and thermal variance dissipation quantify the losses of energy to the environment and concurrently serve as convenient measures of wake

persistence. The decay rate can be calculated by fitting the dissipation rates for each simulation with power laws:

$$\varepsilon = C_\varepsilon (Nt)^{-\lambda_\varepsilon}, \tag{14}$$

$$\chi = C_\chi (Nt)^{-\lambda_\chi}, \tag{15}$$

where (C_ε, C_χ) and $(\lambda_\varepsilon, \lambda_\chi)$ are fit parameters for the turbulent dissipation rate and the thermal variance dissipation rate, respectively. These parameters are estimated from $Nt >$ 1 and $Nt > 4$ for turbulent dissipation rate and thermal variance dissipation rate, respectively, when the dissipation rates begin to resemble power-law decay. Exceptions are made for Case 5 in Fr = 1.0 and Case 3 in Fr = 3.2 in which $Nt > 10$ has been chosen as these simulations show some later variability that might skew the power law fit. The delay in the maximum for χ is caused by the delay for turbulent mixing to impact the temperature. The values of λ_ε and λ_χ are shown in Table 3 for all simulations. In our simulations, decay rates for both sets have comparable values but are only slightly lower than Spedding's (1997) predictions, who found through dimensional arguments that a -7/3 power-law would be expected.

Using λ_ε and λ_χ for each case, we can estimate the turbulent and thermal signal decay until it becomes low enough to be undetectable. Table 4 shows the maximum time that turbulent and thermal signals remain detectable after their generation at $Nt = 0$. We use a minimum level for detection of 10^{-10} W/kg for turbulent dissipation, and 10^{-10} °C^2/s for thermal variance dissipation measurements, as consistent with general instrumentation limits (Peterson and Fer 2014). In general, the background gradient has little effect on the maximum time at which the turbulent dissipation rate may be detected, but it can substantially affect detection time of the thermal dissipation rate. This is especially true at low Fr, giving maximum detection times that are roughly four to five times greater than those for the simulations with Fr = 3.2. In our estimates, Cases 1 and 2 generally produce the longest detectable values of the thermal dissipation rate, approximately twice the maximum detection time for the Linear Case, and four times that for Case 5. Additionally, Case 4 remains as the strongest thermal signal until approximately 10 hours have elapsed.

Table 3. λ_ε and λ_χ for all simulations.

	Fr = 1.0		Fr = 3.2	
	λ_χ	λ_ε	λ_χ	λ_ε
Linear Case	1.68	1.67	2.14	1.82
Case 1	1.57	1.80	1.61	1.60
Case 2	1.50	1.93	1.37	1.49
Case 3	1.77	1.82	1.50	1.89
Case 4	2.14	1.55	2.50	1.63
Case 5	1.59	2.28	1.79	1.87

Table 4. Maximum time for detecting turbulent and thermal signal.

	Fr = 1.0		Fr = 3.2	
Max detection time (h)	χ	ε	χ	ε
Linear Case	92.2	9.2	17.9	5.0
Case 1	150.0	6.4	35.5	6.8
Case 2	182.6	5.4	44.5	7.7
Case 3	68.4	6.2	59.2	8.2
Case 4	83.4	11.9	24.5	7.3
Case 5	52.5	3.2	13.3	4.9

B. INTERNAL WAVES

A major consequence of the non-uniformity of background stratification is the way it can affect the transmission and reflection of internal waves through the domain. To investigate this, we measure the kinetic energy in the radiated internal waves in each simulation. Therefore, we define the kinetic energy above *Zc*, K_{EA}, and kinetic energy below *Zc*, K_{EB}, as

$$K_{EA} = \frac{1}{2}\int\int_{z=Zc}^{z=50}\int_{x=200}^{x=300} \rho_0(u^2+v^2+w^2)\,dV, \tag{16}$$

$$K_{EB} = \frac{1}{2}\int\int_{z=-75}^{z=Zc}\int_{x=200}^{x=300} \rho_0(u^2+v^2+w^2)\,dV. \tag{17}$$

Since the strongest signals are around the wake core, and its center is not always exactly located along the body path, establishing the horizontal plane at *Zc* mitigates such errors.

The results are shown in Figure 18, in which the kinetic energy in the internal waves is plotted in terms of the ratio of total kinetic energy, RKE, which is the ratio K_{EA} to K_{EB}. It is highlighted that only kinetic energy carried by internal waves is relevant for RKE results since *Zc* divides the energy contained in the wake core exactly in half. The kinetic energy in IW is distributed symmetrically over the domain for most cases, although some cases with Fr = 3.2 have most of the energy concentrated in the upper region (z > *Zc*). However, the behavior of Cases 1–3 is highly sensitive to the values of Fr. In Fr = 1.0 cases, the signal above 20 m is very low, as though some barrier prevented internal waves from propagating upward. For Fr = 3.2, the signal is more intense above that level, even though it still substantially diminishes near the surface. To understand this phenomenon, we investigate how internal waves are transmitted and reflected for both Fr sets. The IW energy distribution shown in Figure 18 suggests that internal waves preferentially travel downward for the simulations with concave stratification patterns.

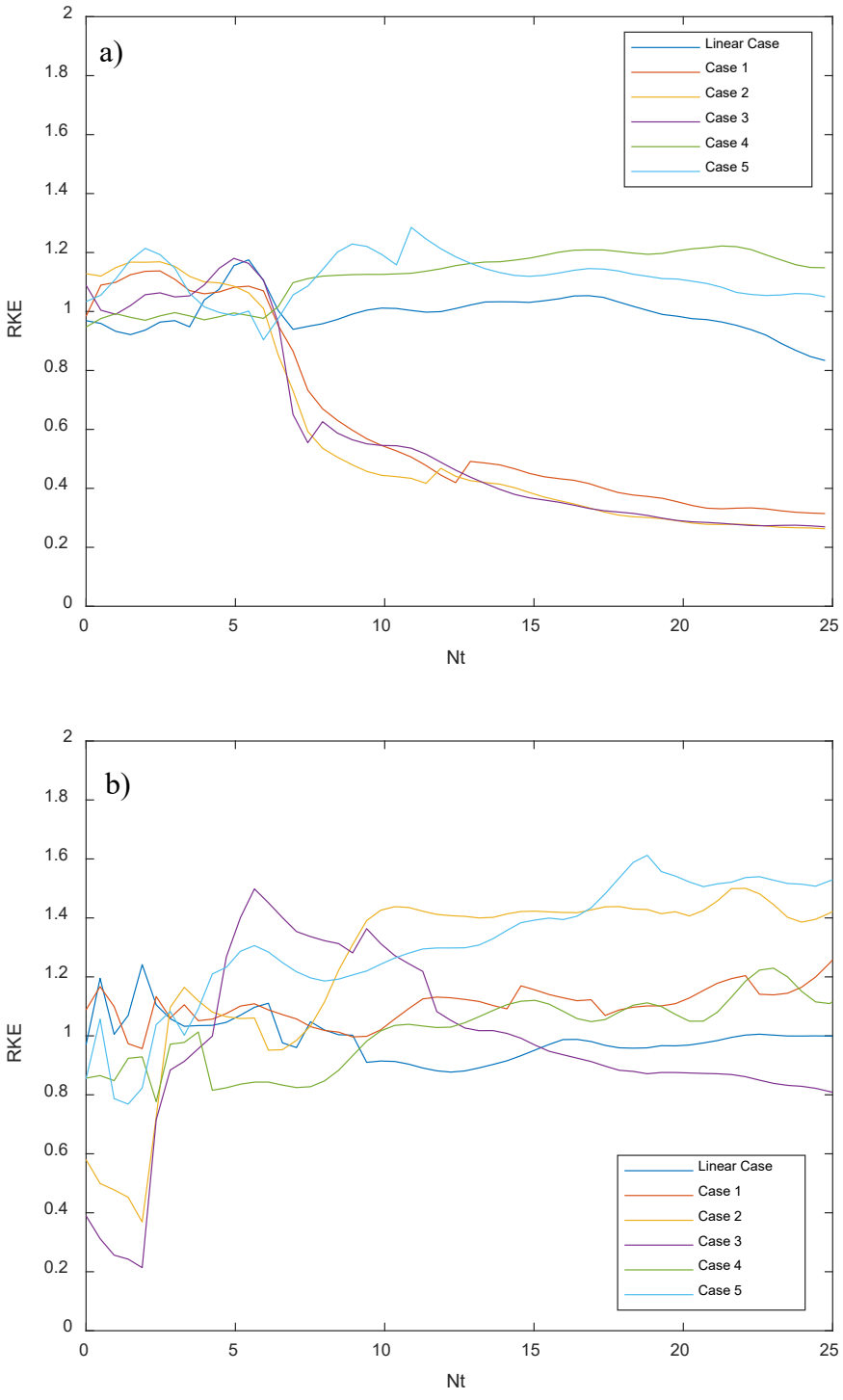

RKE for a) Fr = 1.0, and b) Fr = 3.2.

Figure 18. RKE.

Figure 19 shows vertical cross-sections of the thermal dissipation rate along with the corresponding profiles of the buoyancy frequency for Cases 1–3 with Fr = 1.0. It is evident that there are few internal waves in regions of lowest Brunt- frequency. We can understand this by considering an idealized model for internal wave propagation in two dimensions with fixed stratification:

$$(N^2(z) - \omega^2)\frac{\partial^2}{\partial y^2}w = \omega^2\frac{\partial^2}{\partial z^2}w, \tag{18}$$

where $N(\mathrm{z})$is the buoyancy frequency, which can change with depth, w is the vertical velocity field, and ω is the angular frequency of the internal wave. We assume solutions of the form

$$w = A(z)e^{ik_y y}, \tag{19}$$

where A is the z-dependent amplitude of the internal wave and k_y is the constant horizontal wavenumber. It is clear from these expressions that the solutions depend only on the ratio between N^2 and ω^2. For constant stratification, valid wave solutions only exist when $N^2 - \omega^2 > 0$. Thus, for a localized disturbance at $z = 0$ waves generated far from the disturbance will have angular frequencies in the range of $-N < \omega < N$. For internal waves to transmit, $\frac{N^2}{\omega^2}$must exceed unity on scales larger than $\frac{2\pi}{\mathrm{k_z}}$; otherwise, any evanescent waves will be unable to penetrate the region. This serves to provide an upper bound on waves expected to transmit for a given expression of N^2. For a typical Gaussian perturbation,

$$T = rz + \gamma e^{-\frac{z^2}{\sigma^2}}, \tag{20}$$

we define an ambient buoyancy frequency of $N_0^2 = \alpha g r$ and can therefore represent the internal wave angular frequency as $\omega = aN_0$, where $0 < a < 1$. This results in an expression for their ratio given by

$$\frac{N^2}{\omega^2} = \frac{N^2}{a^2 {N_0}^2} = \frac{1}{a^2} - \frac{2\gamma z}{a^2 r \sigma^2} e^{\frac{-z^2}{\sigma^2}}, \tag{21}$$

and this limits the range of a that can be transmitted to

$$a_{max}^2 = 1 - \frac{\gamma}{r\sigma} \max\left(2\hat{z}e^{-\hat{z}^2}\right), \tag{22}$$

where $\hat{z} = \frac{z}{\sigma}$. The maximum of $2\hat{z}e^{-\hat{z}^2}$ is a constant that must be found numerically and, therefore, so too must a_{max}.

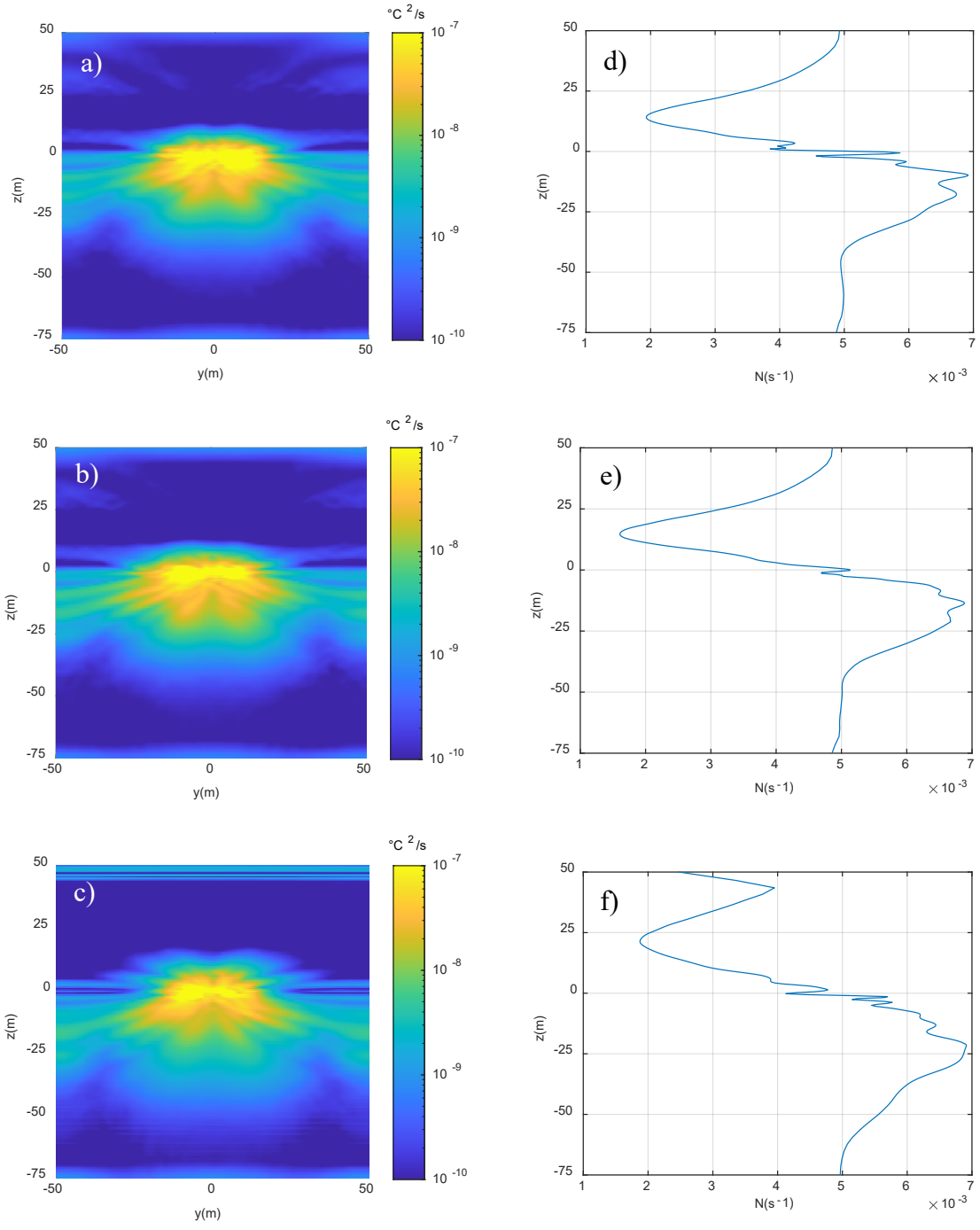

The cross-sections of the thermal dissipation rate for a) Case 1; b) Case 2; and c) Case 3 for Fr = 1.0, and d) *N* profile for Case 1; e) *N* profile for Case 2; and f) *N* profile for Case 3.

Figure 19. Relationship between Brunt-Vaisala frequency profile and the presence of internal waves.

To determine the transmission coefficient, we numerically integrate the amplitude of the internal wave from a distant point in $-z$ (-10σ) to a corresponding point in $+z$ (10σ)given an initial value of A and A', the z-derivative of A. We consider that the wave amplitude at the start, $A(-10\sigma)$, is the sum of the incident (assumed to have an amplitude of unity) and reflected waves (with an amplitude of R), and the wave amplitude at the end, $A(10\sigma)$ is the amplitude of the transmitted wave (with an amplitude of Y). This means that the initial form of A would be well approximated by

$$A(z) = e^{ik_z z} + Re^{-ik_z z}, \tag{23}$$

and the final form by

$$A(z) = Ye^{ik_z z}. \tag{24}$$

However, it is difficult to ascertain a priori the correct complex value of R such that the transmitted wave contains no $e^{-ik_z z}$ component. Thus, we evolve two independent waves with initial values of A and A' given by $A = e^{\pm ik_z z}$, and yielding two final values (and derivatives) of A, which we denote as $A_{\pm}$ (and $A'_{\pm}$). To determine the correct value of R, we can construct a linear combination of A_- and A_+ such that Equation (24) holds true. Each result of the numerical integration yields a final value of A, which can be expressed in terms of the forward and backward propagating solutions:

$$A_{\pm}(\mathrm{z}) = F_{\pm}e^{ik_z z} + B_{\pm}e^{-ik_z z}, \tag{25}$$

and the amplitude of the backward propagating solution is then calculated from

$$B_{\pm} = e^{ik_z z}\left(A_{\pm} - \frac{1}{ik_z}A'_{\pm}\right). \tag{26}$$

For this to be a valid solution, then, the final state is given by

$$A(z) = F_+ e^{ik_z z} + B_+ e^{-ik_z z} + RF\_e^{ik_z z} + RB\_e^{-ik_z z}, \quad (27)$$

where we require $B_+ + RB_- = 0$, so that there is no backward-propagating solution in the transmission region. The magnitude of the reflection coefficient is then simply

$$|R| = \frac{|B_+|}{|B_-|}. \quad (28)$$

Thus, the relationship of the horizontal wavenumber to the coefficient a, which can be shown to be $\cos\theta$, where θ is the IW horizontal angle, is obtained from the areas where IW propagating upwards should not pass, and consequently, they will be reflected. Figure 20 shows the reflection coefficient for Cases 1–3 as a function of horizontal wavenumber and $\cos\theta$. Large values of $\cos\theta$ are reflected, and low values are transmitted. However, the value of a_{max} can also be seen on the plot as the place where R~0.5. Nevertheless, decreasing k_y also decreases k_z for a given horizontal angle, and the interactions between the Gaussian and the wave can partially transmit in a certain range of horizontal angles.

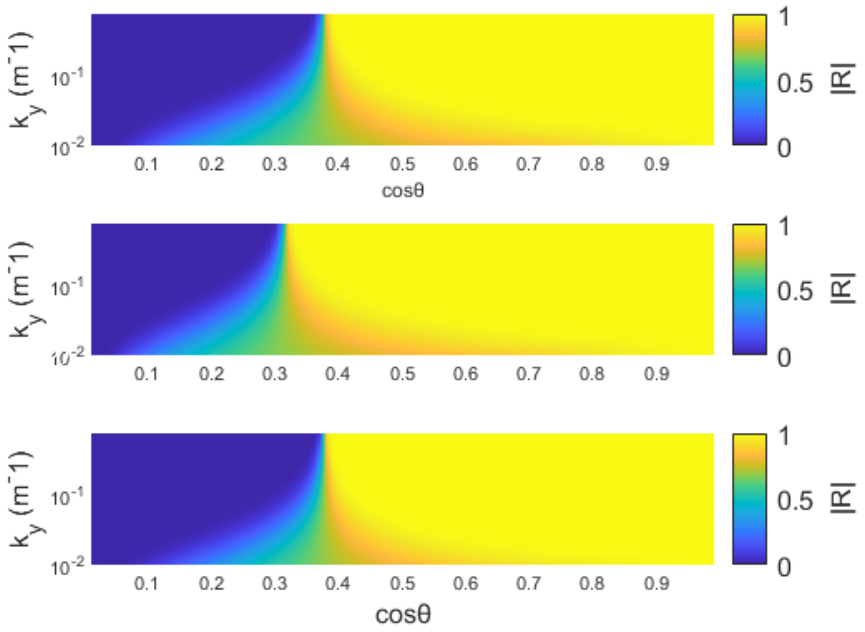

The reflectivity index based on the relation between horizontal wavenumber, k_y, and $cos\theta$ for a) Case 1, b) Case 2, and c) Case 3.

Figure 20. Reflection coefficient.

As we have seen, conditions for transmission through weakly stratified areas depend on the wavelength and the direction of propagation, typical values of which can depend on Fr. Internal waves are emitted in a broad frequency range, and the two types of IW radiated from a wake are lee and random waves. Meunier et al. (2018) experimentally showed that large lee waves occur at early stages, from Nt = 0 to 30, whereas small wake waves are more important in later stages, from Nt = 30 to 150. Therefore, we can infer that the waves being reflected are mainly lee waves. Since these waves have roughly the same speed as the speed of the body, u_b, and the medium oscillates at $f = \frac{N}{2\pi}$, the IW wavelength in the x direction, which is described as $U = L_x f$, can be also expressed as $L_x = 2\pi D\mathrm{Fr}$ (Meunier et al. 2018), so we expect the wavelength to increase with Fr. From Figure 20 we notice that, in general, as wavenumber decreases, a smaller range of angles is susceptible to total reflection, but the magnitude of wavenumber should be determined for each Fr to ascertain how significant that difference is when comparing the range of fully reflective IW angles of the two Fr.

To obtain a more accurate prediction of the amount of energy reaching the top, it is also necessary to estimate the angular distribution of energy carried by the IW for each case. In Figure 21, we show the specific kinetic energy contained by internal waves propagating for various angles for the two Linear Case experiments at Nt = 10, and these measurements are made at a 30-m radius around the x-axis. Rowe et al. (2020) found that the contribution of kinetic energy radiated for $10 \leq Nt \leq 25$ is significant and internal waves are broadcast across a wider range of angles. Therefore, Nt = 10 is chosen as representative of the range of IW horizontal angle. For Fr = 1.0, the specific kinetic energy conducted by IW at steeper horizontal angles is very low and the peaks of energy are radiated at shallower angles. Conversely, for Fr = 3.2, the amount of energy propagated by IW at steeper horizontal angles is much larger than in the Fr =1.0 Case. In addition, it is possible to calculate the magnitude of the wavelength, L, by measuring the distance between the peaks of IW energy and then decomposing in the z and y directions, L_z and L_y, respectively, according to the mean horizontal angle of the two most energetic consecutive wavefronts, θ_1 and θ_2. The values of L_y, L_z, k_y, k_z, θ_1, and θ_2 are shown in Table 5. Estimated ranges of horizontal angles at which internal waves are likely reflected

can also be made from the idealized transmission model using the values previously determined for k_y. For Fr = 3.2, the range of horizontal angles liable to be reflected are only a little smaller than for Fr = 1.0, 60 degrees for Fr = 3.2, and 64 degrees for Fr = 1.0, considering the slightly smaller k_y for the highest Fr. Since the most energetic IW are being irradiated at horizontal angles less than 60°, and only very few IW are radiated at steeper angles in Fr = 1.0, we would expect more reflection in this case. Therefore, we can conclude that more energy should be transmitted and reach the top in Fr = 3.2 cases due to the steeper angles of IW emissions.

Table 5. Estimated internal waves parameters.

	L_y (m)	L_z(m)	$k_y(\mathrm{m}^{-1})$	$k_z(\mathrm{m}^{-1})$	$\theta_1(°)$	$\theta_2(°)$
Fr = 1.0	9.3	7	1.1×10^{-1}	1.4×10^{-1}	53	30
Fr = 3.2	11.4	6.6	8.7×10^{-2}	1.5×10^{-1}	60	34

a)

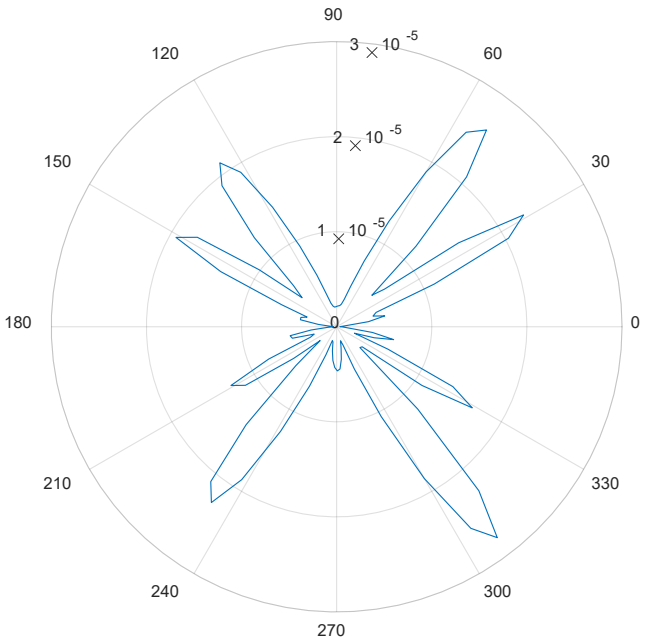

b)

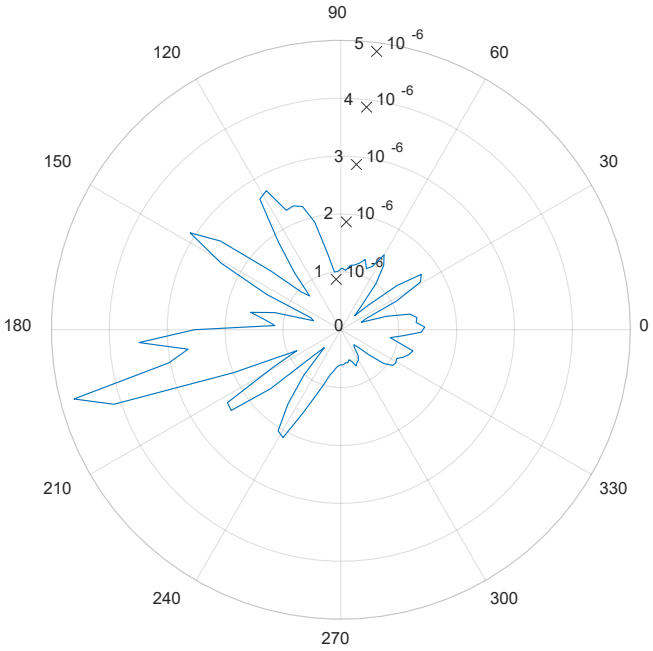

Specific kinetic energy carried out by internal waves versus the horizontal angle of IW emissions for the Linear Cases with a) Fr = 1.0 and b) Fr = 3.2, when Nt = 10.

Figure 21. Distribution of specific kinetic energy emitted by IW as a function of the propagation angles.

IV. DISCUSSION

A. CONCLUSIONS

This study is focused on the dynamics of turbulent wakes generated by submerged objects moving through a stratified fluid with a nonlinear background temperature profile. This investigation reveals the major impacts of stratification anomalies on the wake strength, position, signal, and energy distribution. We note that patterns of the turbulent and thermal dissipation rates show asymmetric distribution of the internal waves emitted by the propagating object, which is attributed to non-uniformities of stratification. This effect is particularly noticeable for concave profiles and low Fr. The dependence on Fr is due to the shallower range of IW radiation angles emitted from wakes at low Fr which are more easily reflected. For higher Fr, steeper IW emissions allow more IW to pass through areas of low stratification. The wake core position is also dependent on the background stratification. In stronger stratifications, the wake core remains near the original path of the object, while in weaker stratifications, the wake core can drift substantially.

Investigating estimated decay rates of ε and χ, it is possible to measure how long these quantities will be detectable. Results have shown that thermal signals are very sensitive to total background stratification as well as temperature perturbations. In general, the maximum detection time is higher for stronger stratification, and concave anomalies remain the longest detectable signal, whereas typical mixed-layer profiles have the shortest. Wake signatures for low Fr are substantially longer than those for higher Fr. In addition, concave profiles have signatures that are longer than uniform linear stratification. The turbulent dissipation rate in the wake decays substantially in time, which limits the ability to detect the wake directly. Furthermore, we do not find much variability in the maximum detection time for such signals, showing that it is not significantly affected by perturbations in stratification.

B. OPERATIONAL RELEVANCE

To inform the operational community of relevant wake properties, we have analyzed signal strength and maximum signal detection time. We have demonstrated that

regions with sharp temperature changes greatly facilitate thermal signal detection. In such areas, thermal signatures remain detectable for roughly 9 to 11 hours after the wake is generated. The maximum time for detection of turbulent signals is comparable for all cases and is predicted to be within 3 to 12 hours, exhibiting very limited sensitivity to nonlinear temperature perturbations. Thermal signals, though, vary substantially depending on the stratification pattern. For strong stratification, the maximum detection time is much longer than for weak stratification, approximately 52–182 hours for strong stratification, and 13–45 hours for weak stratification. Furthermore, concave stratifications show the longest detection time, ranging up to 182 hours. Some concave profiles have substantially longer detection time than uniform stratification, for which detection may be possible up to 92 hours after passage. Mixed-layer type perturbations have the shortest detection times, and the maximum detection time can be as short as 13 hours in weaker stratification.

C. FUTURE WORK

This research is a gateway to further advances in the observations of turbulent wakes in stratified environments. Since the ocean harbors a wide variety of density patterns, new types of nonlinear profiles could be simulated, accounting for salinity anomalies. Future research project should prioritize the analysis of profiles acquired from areas of the most strategic interest. Laboratory or field experiments could be conducted to validate the results obtained from simulations. Laboratory experiments could be set up with a complex temperature field, through which a small body could be towed, as in Danieletto et al. (2019). The results from such experiments could be compared to the corresponding simulations. Another potentially profitable approach would be to use data for simulations from field experiments already conducted, such as the work done in Monterey Bay by Moody et al. (2017).

APPENDIX. TEMPERATURE PROFILES SYMMETRY

We begin with the Boussinesq equations for a single-component fluid, decomposing the temperature according to $T(t,x,y,z) + (\partial\overline{T_0}/\partial z)\, z + \overline{T_1}(t,z)$, where $\partial\overline{T_0}/\partial z$ is a constant, $\overline{T_1}(t,z)$ is the predetermined initial deviation away from the uniform temperature gradient that can evolve in time, and T is the thermal perturbation:

$$\frac{\partial \mathbf{u}}{\partial t} + \mathbf{u}\cdot\nabla\mathbf{u} = -\frac{\nabla p}{\rho_0} + \alpha g(T + \overline{T_1})e_z + \nu\nabla^2\mathbf{u}, \tag{29}$$

$$\frac{\partial(T + \overline{T_1})}{\partial t} + \mathbf{u}\cdot\nabla(T + \overline{T_1}) + w\frac{\partial T_0}{\partial z} = k_T\nabla^2(T + \overline{T_1}), \tag{30}$$

$$\nabla\cdot\mathbf{u} = 0. \tag{31}$$

In the absence of motion, the thermal equation becomes

$$\frac{\partial \overline{T_1}}{\partial t} = k_T\nabla^2(\overline{T_1}), \tag{32}$$

which we can subtract from Equation 23 to yield

$$\frac{\partial T}{\partial t} + \mathbf{u}\cdot\nabla T = -w\frac{\partial \overline{T_0}}{\partial z} - w\frac{\partial \overline{T_1}}{\partial z} + k_T\nabla^2 T. \tag{33}$$

Cases 1–3 and their symmetric profiles are equivalent to a Gaussian $\overline{T_1}$ with a positive and negative amplitude, respectively; thus, we consider a (primed) system with $\overline{T'_1}(t,z) = -\overline{T_1}(t,-z)$. Assuming that u, v, ω, p, and T are a solution for $\overline{T_1}(t,z)$, we will show that the following

$$u'(t,x,y,z) = u(t,x,y,-z), \tag{34}$$

$$v'(t,x,y,z) = v(t,x,y,-z), \tag{35}$$

$$w'(t,x,y,z) = -w(t,x,y,-z), \tag{36}$$

$$p'(t,x,y,z) = p(t,x,y,-z), \tag{37}$$

$$T'(t,x,y,z) = -T(t,x,y,-z), \tag{38}$$

form a solution for $\overline{T'_1}(t,z)$. For the continuity equation, this would require

$$\nabla\cdot\mathbf{u}'^{(t,x,y,z)} = \frac{\partial u(t,x,y,-z)}{\partial x} + \frac{\partial v(t,x,y,-z)}{\partial y} + \frac{\partial\big(-w(t,x,y,-z)\big)}{\partial z} = 0. \tag{39}$$

Under the transformation of $\mathrm{z}' = -\mathrm{z}$, this becomes

$$\frac{\partial u(t,x,y,\mathrm{z}')}{\partial x}+\frac{\partial v(t,x,y,\mathrm{z}')}{\partial y}-\frac{\partial(-w(t,x,y,\mathrm{z}')}{\partial \mathrm{z}'}=0, \tag{40}$$

which is equivalent to the original continuity equation with z' instead of z. From this point on, all discussion will be for variables in the (t,x,y,z') coordinate transformation and the coordinates will be dropped for convenience. We can treat the temperature equation in a similar way to the continuity equation, finding

$$-\frac{\partial T}{\partial t}+\mathbf{u}\frac{\partial(-T)}{\partial x}+v\frac{\partial(-T)}{\partial \mathrm{y}}-(-w)\frac{\partial(-T)}{\partial z'}=w\frac{\partial \overline{T_0}}{\partial z}-w'^{\frac{\partial(-\overline{T_1})}{\partial z'}}-k_T\nabla'^2T, \tag{41}$$

where we have denoted $\nabla'\equiv\left(\frac{\partial}{\partial \mathrm{x}},\frac{\partial}{\partial \mathrm{y}},\frac{\partial}{\partial \mathrm{z}'}\right)$and where we recognize that $\frac{\partial\overline{T_0}}{\partial \mathrm{z}}$is a constant parameter of the system. Again, this is equivalent to the original temperature evolution equation. We note that converting the Laplacian to the primed coordinate system (∇'^2) does not cause a change of sign since

$$\left(-\frac{\partial}{\partial z'}\right)\left(-\frac{\partial}{\partial z'}\right)=\frac{\partial^2}{\partial \mathrm{z}'^2}. \tag{42}$$

The components of the momentum equation for the primed solution can be shown to be equivalent to the original equation components by the same method:

$$\frac{\partial u}{\partial t}+u\frac{\partial u}{\partial x}+v\frac{\partial u}{\partial y}-(-w)\frac{\partial u}{\partial z'}=-\frac{1}{\rho_0}\frac{\partial p}{\partial x}+\nu\nabla'^2u, \tag{43}$$

$$\frac{\partial u}{\partial t}+u\frac{\partial u}{\partial x}+v\frac{\partial u}{\partial y}-(-w)\frac{\partial u}{\partial z'}=-\frac{1}{\rho_0}\frac{\partial p}{\partial y}+\nu\nabla'^2v, \tag{44}$$

$$-\frac{\partial w}{\partial t}+u\frac{\partial(-w)}{\partial x}+v\frac{\partial(-w)}{\partial y}-(-w)\frac{\partial(-w)}{\partial z'}=-\frac{1}{\rho_0}\frac{\partial p}{\partial z'}+\alpha g(-T-\overline{T_1})-\nu\nabla'^2w. \tag{45}$$

In summary, this shows that if a solution to the Boussinesq equations exists for an initial temperature field of $\left(\frac{\partial\overline{T_0}}{\partial \mathrm{z}}\right)\mathrm{z}+\overline{T_1}(0,z)$, then a mirrored system with initial condition $\left(\frac{\partial\overline{T_0}}{\partial \mathrm{z}}\right)\mathrm{z}-\overline{T_1}(0,-z)$ will have the same solution only mirrored around $\mathrm{z}=0$ and with the thermal perturbation and vertical velocity of opposite sign.

LIST OF REFERENCES

Abdilghanie, A., and P. Diamessis, 2013: The internal gravity wave field emitted by a stably stratified turbulent wake. *J. Fluid Mech.,* **720**, 104–139, https://doi.org/10.1017/jfm.2012.640.

Brucker, K., and S. Sarkar, 2010: A comparative study of self-propelled and towed wakes in a stratified fluid. *J. Fluid Mech.*, **652**, 373–404, https://doi.org/10.1017/S0022112010000236.

Bureau of Naval Personnel, 1953: Transmission of sound in sea water. *Naval sonar*, United States Government Printing Office, 32–51.

Danieletto M., J.M. Brown, T. Radko, 2019: The Immortal Science of Dead Water: Effects of Internal Wave Drag on Propagating Submerged Bodies. *J Oceanogr Mar Res*, **7:**191. doi: 10.4172/2572-3103.1000191.

De Stadler, M., 2013: High resolution simulation of the turbulent wake behind a sphere in a stratified fluid. Ph.D. dissertation, Dept. of Engineering Science, University of California San Diego, 241 pp.

Diamessis, P. J., G. R. Spedding, and J. A. Domaradzki, 2011: Similarity scaling and vorticity structure in high-Reynolds-number stably stratified turbulent wakes. *J. Fluid Mech.*, **671**, 52–95, https://doi.org/10.1017/S0022112010005549.

Gilreath. H. E., and A. Brandt, 1985: Experiments on the generation of internal waves in a stratified fluid. *AIAA Journal*, **23**, 693–700, https://doi.org/10.2514/3.8972.

Gregg, M. C., E. A. D'Asaro, J. J. Riley, and E. Kunze, 2018: Mixing efficiency in the ocean. *Annu. Rev. Marine Science*, **10**, 443–473. https://doi.org/10.1146/annurev-marine-121916-063643.

Holzmann, T., 2019: The numerical algorithms: SIMPLE, PISO and PIMPLE. *Mathematics, numerics, derivations and OpenFOAM®*, Holzmann CFD, 93–123.

Hopfinger, E. J., J. B. Flor, J. M. Chomaz, and P. Bonneton, 1991: Internal waves generated by a moving sphere and its wake in a stratified fluid. *Experiments in Fluids*, **11**, 255–261, https://doi.org/10.1007/BF00192753.

Keller, J. B., and W. H. Munk, 1970: Internal wave wakes of a body moving in a stratified fluid. *Physics of Fluids*, **13**, 1425, https://doi.org/10.1063/1.1693096.

Lin, J. T., and Y. H. Pao, 1979: Wakes in stratified fluids. *Annu. Rev. Fluid Mech.*, **11**, 317–338, https://doi.org/10.1146/annurev.fl.11.010179.001533.

Meunier, P., S. Le Dizès, L. Redekopp, and G. R. Spedding, 2018: Internal waves generated by a stratified wake: Experiment and theory. *J. Fluid Mech.*, **846**, 752–788, https://doi.org/10.1017/jfm.2018.278.

Meunier, P., and G. R. Spedding, 2004: A loss of memory in stratified momentum wakes. *Physics of Fluids*, **16**, 298–305, https://doi.org/10.1063/1.1630053.

Moody, Z., C. Merriam, T. Radko, and J. Joseph, 2017: On the structure of stratified wakes generated by submerged propagating objects. *J. Operational Oceanogr.*, **10**, 191–204, https://doi.org/10.1080/1755876X.2017.1307801.

OpenFOAM®, 2012. *The Open Source CFD Toolbox, User Guide v2012*. https://www.openfoam.com/documentation/guides/v2012/doc/.

Pao, Y.-H., 1973: Measurements of internal waves and turbulence in two-dimensional stratified shear flows. *Boundary-Layer Meteor.*, **5**, 177–193 https://doi.org/10.1007/BF02188318.

Pao, H. P., Y. L. Robert, and E. S. Charles, 1982: Vortex trails in stratified fluids. *Johns Hopkins APL Technical Digest*, **3**, 12–18.

Peterson, A. K., and I. Fer, 2014: Dissipation measurements using temperature microstructure from an underwater glider. *Methods in Oceanogr.*, **10**, 44–69, https://doi.org/10.1016/j.mio.2014.05.002.

Radko, T., and D. Lewis, 2019: The age of a wake. *Physics of Fluids*, **31**, 076601. https://doi.org/10.1063/1.5100969.

Radko, T., and D. Lorfeld, 2018: Effects of weak planetary rotation on the stability and dynamics of internal stratified jet. *Physics of Fluids*, **30**, 096602. https://doi.org/10.1063/1.5049598

Redford, J. A., T. S. Lund, and G. N. Coleman, 2015: A numerical study of a weakly stratified turbulent wake. *J. Fluid Mech.*, **776**, 568–609, https://doi.org/10.1017/jfm.2015.324.

Riley, J.J., and M.P. Lelong, 2000: Fluid motions in the presence of strong stable stratification. *Annu. Rev. Fluid Mech.*, **32**, 613–657, https://doi.org/10.1146/annurev.fluid.32.1.613.

Rottman, J. W., D. Broutman, G. Spedding. and P. Meunier, 2004: The internal wave field generated by the body and wake of a horizontally moving sphere in a stratified fluid. *Proc. 15th Australasian Fluid Mech. Conf.,* Sydney, Australia.

Rowe, K. L., P. J. Diamessis, and Q. Zhou, 2020: Internal gravity wave radiation from a stratified turbulent wake. *J. Fluid Mech.*, **888**, A25, https://doi.org/10.1017/jfm.2020.40.

Spedding, G. R., 1997: The evolution of initially turbulent bluff-body wakes at high internal Froude number. *J. Fluid Mech.*, **337**, 283–301, https://doi.org/10.1017/S0022112096004557.

Spedding, G. R., 2014: Wake signature detection. *Annu. Rev. Fluid Mech.*, **46**, 273–302, https://doi.org/10.1146/annurev-fluid-011212-140747.

Sutyrin, G. G., and T. Radko, 2017: The fate of pancake vortices. *Physics of Fluids*, **29**, 031701, https://doi.org/10.1063/1.4977975.

Tisovska, P., 2019: Description of the overset mesh approach in ESI version of OpenFOAM. *Proc. CFD with Open-Source Software*, H. Nilsson. Ed, http://dx.doi.org/10.17196/OS_CFD#YEAR_2019.

Weller, H. G., G. Tabor, H. Jasak, and C. Fureby, 1998: A tensorial approach to computational continuum mechanics using object-oriented techniques. *Computers in Physics*, **12**, 620–631, https://doi.org/10.1063/1.168744.

Xu, Y., H. J. S. Fernando, and D. L. Boyer, 1995: Turbulent wakes of stratified flow past a cylinder. *Physics of Fluids*, **7**, 2243, https://doi.org/10.1063/1.868472.

Zhou, Q., and P. J. Diamessis, 2019: Large-scale characteristics of stratified wake turbulence at varying Reynolds number. *Phys. Rev. Fluids*, **4**, 084802. https://doi.org/10.1103/PhysRevFluids.4.084802.

Zhou, Q., and P. Diamessis, 2016: Surface manifestation of internal waves emitted by submerged localized stratified turbulence. *J. Fluid Mech.*, **798**, 505–539, https://doi.org/10.1017/jfm.2016.342.

THIS PAGE INTENTIONALLY LEFT BLANK

INITIAL DISTRIBUTION LIST

1. Defense Technical Information Center
   Ft. Belvoir, Virginia

2. Dudley Knox Library
   Naval Postgraduate School
   Monterey, California